Interpretation of forest disturbance using a time series of Landsat imagery and canopy structure from airborne lidar

Oumer S. Ahmed, Steven E. Franklin, and Michael A. Wulder

Abstract. In this study we examined forest disturbance, largely via forest harvest, over three decades in a coastal temperate forest on Vancouver Island, British Columbia, Canada. We analysed how disturbance history relates to current canopy structural conditions by interpreting the relationship between light detection and ranging (lidar) derived canopy structure and forest disturbance trajectories derived from Landsat images to assess if a particular stand structural condition is to result based on disturbance histories. The lidar data were obtained in 2004, and are used to relate forest structural conditions at the end of the Landsat time series (1972–2004), essentially providing for a measure of resultant structure emerging from the spectral trends captured. Correlation analysis was applied between lidar-derived canopy structure (canopy cover and height) and Landsat spectral indices, such as the Tasseled Cap Angle (TCA), which showed a strong correlation coefficient ($r = 0.86$) with canopy cover. TCA was then used to characterize change in forest disturbance through the full temporal depth of the available Landsat image time series using a trajectory-based characterization method. Approximately 71.5% of the study area was found to correspond to "stable and undisturbed forest". Four disturbance classes (areas characterized by disturbance, disturbance followed by revegetation, ongoing revegetation, and revegetation to stable state) accounted for approximately 10.2%, 5.3%, 2.2%, and 10.5% of the study area, respectively. We evaluated the forest structural and spectral separability between the disturbance classes. In terms of structural variability the mean airborne lidar-derived canopy cover showed clear differentiation between disturbance classes. Spectral mixture analysis (SMA) was used to extract the spectral characteristics for each disturbance class. The SMA-derived fractions were then used to analyse the class separability between the Landsat trajectory derived disturbance classes. The fraction images provided clear distinction between disturbance classes in abundances between sunlit canopy, non-photosynthetic vegetation, shade, and exposed soil. The extracted spectral indices and SMA fractions within the Landsat trajectory derived disturbance classes were used to assess if terminal forest structural conditions can be related to a complex suite of stand development trajectories and processes. The Landsat spectral indices and SMA fractions were separately modeled to estimate lidar-derived mean canopy cover and height data within each disturbance class using multiple regression. The results indicate canopy cover and height regression models developed using spectral indices provided a relatively better estimation than those using SMA endmember fractions. Compared with the relatively regular structure of fully grown undisturbed (stable) forests, the forest disturbance classes typically exhibited complex irregular structure, making it more difficult to accurately estimate their canopy cover and height. As a result, all models developed for the stable forest class performed better than those developed for other forest disturbance classes. Modeling canopy cover and height from Landsat temporal spectral indices resulted in modeled agreement to lidar measures of R^2 0.82 (RMSE 0.09) and R^2 0.67 (RMSE 3.21), respectively. Our results also indicate moderately accurate predictions of lidar-derived canopy height can be obtained using the Landsat-level disturbance class endmember fractions with R^2 0.60 and RMSE 4.19. This study demonstrates the potential of using the over four decade record of Landsat observations (since 1972) to estimate forest canopy cover and height using prestratification of the data based on disturbance trajectories.

Résumé. Dans cette étude, nous examinons la perturbation des forêts, liée en grande partie à l'exploitation forestière, pendant trois décennies dans une forêt tempérée côtière sur l'île de Vancouver, Colombie-Britannique, Canada. Nous avons analysé comment l'historique des perturbations est lié aux conditions structurelles du couvert forestier actuel par l'interprétation de la relation entre la structure du couvert forestier dérivée du lidar («light detection and ranging») et les trajectoires des perturbations forestières dérivées d'images Landsat pour évaluer si la condition structurelle d'un

Oumer S. Ahmed[1]. Geomatics, Remote Sensing and Land Resources Laboratory, Department of Geography, Trent University, ON, K9J 7B8, Canada.

Steven E. Franklin. Department of Environmental and Resource Studies/Science, Department of Geography, and Office of the President, Trent University, ON, K9J 7B8, Canada.

Michael A. Wulder. Canadian Forest Service (Pacific Forestry Centre), Natural Resources Canada, 506 West Burnside Road, Victoria, BC, V8Z 1M5, Canada.

[1]Corresponding author: (e-mail: osahmed@trentu.ca)

peuplement résulte de l'historique des perturbations. Les données lidar ont été obtenues en 2004, et sont utilisées pour relier les conditions structurelles forestières à la fin de la série temporelle Landsat (1972–2004), fournissant essentiellement une mesure de la structure résultante des tendances spectrales capturées. Une analyse de corrélation a été appliquée entre la structure du couvert forestier dérivée du lidar (la couverture de la canopée et la hauteur) et des indices« spectraux Landsat, tel le «Tasseled Cap Angle» (TCA), qui a montré un fort coefficient de corrélation ($r = 0.86$) avec la couverture de la canopée. Le TCA a ensuite été utilisé pour caractériser des changements de la perturbation des forêts sur toute la série temporelle d'images Landsat disponible en utilisant une méthode de caractérisation basée sur des trajectoires. Environ 71,5% de la zone d'étude a été identifiée comme correspondant à de la « forêt stable et non perturbée ». Quatre classes de perturbations (zones caractérisées par une perturbation, une perturbation suivie par le reverdissement, un reverdissement en cours et un reverdissement arrivé l'état stable) représentaient respectivement environ 10,2%, 5,3%, 2,2% et 10,5% de la zone d'étude. Nous avons évalué la séparabilité structurelle et spectrale de la forêt entre les classes de perturbations. En termes de variabilité structurelle, la couverture moyenne de la canopée obtenue du lidar aéroporté a montré une différenciation claire entre les classes de perturbations. L'analyse des mélanges spectraux (SMA) a été utilisée pour extraire les caractéristiques spectrales pour chaque classe de perturbations. Les fractions obtenues par SMA ont ensuite été utilisées pour analyser la séparabilité des classes entre les classes de perturbations dérivées des trajectoires Landsat. Les images de fraction ont fourni une distinction claire entre les classes de perturbations dans les abondances entre le couvert forestier ensoleillé, la végétation non photosynthétique, l'ombre et les sols non couverts. Les indices spectraux extraits et les fractions SMA dans les classes de perturbations dérivées des trajectoires Landsat ont été utilisés pour évaluer si les conditions structurelles finales de la forêt peuvent être liées à un ensemble complexe de trajectoires et processus de développement des peuplements. Les indices spectraux Landsat et les fractions SMA ont été modélisés séparément pour estimer les données de couverture moyenne de la canopée et la hauteur dérivée du lidar au sein de chaque classe de perturbations en utilisant une régression multiple. Les résultats montrent que les modèles de régression de la couverture de la canopée et de la hauteur développés en utilisant les indices spectraux fournissent une meilleure estimation que ceux utilisant des fractions de composantes spectrales pures («endmember») du SMA. Comparées à la structure relativement régulière des forêts à maturité non perturbées (stable), les classes de forêts avec perturbations ont généralement une structure irrégulière et complexe, ce qui rend plus difficile l'évaluation précise de la couverture de la canopée et de la hauteur. En conséquence, tous les modèles développés pour la classe de forêt stable montrent de meilleurs résultats que ceux développés pour les classes perturbées. La modélisation de la couverture de la canopée et de la hauteur en utilisant des indices spectraux temporels de Landsat a permis d'obtenir des R^2 de 0,82 (RMSE 0,09) et 0,67 (RMSE 3,21) respectivement avec les mesures lidar. Nos résultats indiquent également que des prévisions modérément précises de la hauteur de la canopée obtenue à partir du lidar peuvent être obtenues en utilisant les fractions de composantes spectrales pures des classes de perturbations au niveau de Landsat avec R^2 0,60 et RMSE 4,19. Cette étude démontre la possibilité d'utiliser l'archive d'observations Landsat, comprenant plus de quatre décennies (depuis 1972) de données, pour estimer la couverture et la hauteur de la canopée à l'aide de la préstratification des données basées sur des trajectoires de perturbations.
[Traduit par la Rédaction]

Introduction

Forests play a significant role in global terrestrial ecosystems including, but not limited to, providing a carbon sink in the global carbon cycle (Dixon et al., 1994; Goodale et al., 2002), preservation of biodiversity (Dobson et al., 1997), and conservation of soil and water resources (Lal, 1997). Changes in forest structure strongly influence ecosystem processes (Pregitzer et al., 2004), and there is an increasing need to generate accurate information regarding the patterns, rates, and trends of forest dynamics and structural change (Wulder and Franklin, 2007).

Field-based studies of forest ecosystems, while typically of high accuracy, are costly and limited in spatial scales, often providing quality information for a limited number of stands at the landscape scale (Song et al., 2007). Consequently, remote sensing techniques and statistical modeling have been increasingly utilized to assist in forest surveys (McRoberts et al., 2010).

Remotely sensed data are an ideal data source for forest structure change detection (Lu et al., 2004; Kennedy et al. 2007) and are currently the only feasible and cost-effective option for surveying extensive areas (Lunetta et al., 2004).

Satellite remote sensing datasets such as those from the Landsat sensors (Multispectral Scanner (MSS), Thematic Mapper (TM), and Enhanced Thematic Mapper (ETM+)) offer the capacity to relate land cover dynamics and structural characteristics in a systematic, repeatable, and cost effective fashion over long time periods and a variety of spatial scales (Cohen et al., 1998; Cohen and Goward, 2004). The temporal depth and increasingly well-understood radiometric characteristics of such data provide an opportunity to develop more accurate and reliable change detection and analysis methods. The overall goal of such remote sensing studies is to generate valuable information for management, science, and policy objectives. However, the relationship between single-date reflectance and forest structure weakens under certain canopy conditions. The structure and composition of a forest stand at any point in time is linked to the stand's disturbance history. In this research we aim, through use of light detection and ranging (lidar) derived terminal structural conditions and Landsat-derived temporal trajectories, to demonstrate and improve our ability to model key attributes of forest structure. The Landsat-derived temporal trajectories provide otherwise unavailable information

regarding vegetation status and successional history. For instance, Helmer et al. (2010) mapped foliage height profiles with time series of Landsat and Advanced Land Imager imagery in subtropical dry forest where forest height relates strongly to recent and past spectral data; they demonstrated that forest height estimation models that are based only on one image time step result a weaker estimation. In another recent example, Gomez et al. (2011) described the linkages between forest structure and various processes influencing stand condition, development, and disturbance legacy. They showed that forest structural conditions can be related to stand development trajectories and processes, such as regeneration status and rates that are influenced by forest management practices and natural disturbance regimes. Pflugmacher et al. (2012) also demonstrated the utility of disturbance and recovery metrics derived from spectral profiles of annual Landsat time series to predict current forest structure attributes in a mixed-conifer forest. Supported by the opening of the Landsat image archive, recent studies have integrated Landsat-based disturbance history with other remote sensing data such as the Geoscience Laser Altimeter System data to assess forest growth rates (Dolan et al., 2009) and to estimate young forest heights (Li et al., 2011).

Lidar is an active remote sensing system well suited to measure the vertical structure of forests (Hall et al., 2011). Numerous studies have demonstrated that lidar data can be used to accurately estimate forest height and aboveground biomass (Drake et al., 2003), leaf area index (Zhao and Popescu, 2009), canopy density (Donoghue et al., 2007), vertical vegetation strata (Morsdorf et al., 2010), succession stages (Falkowski et al., 2009), and canopy architecture (Andersen et al., 2005). Lidar data work well in small areas and applications that require highly detailed structural information. The analysis of lidar data and Landsat imagery together is promising when larger areas, historical datasets, and a higher temporal resolution are considered (Goetz et al., 2009). Such an approach may also be required to adequately represent and model vegetative content and horizontal structure of forests together with the vertical elements of forest structure (Wulder and Seemann, 2003).

An asymptotic relationship is typically found when using satellite multispectral imagery alone to make empirical estimates of forest structure (Duncanson et al., 2010), with the asymptote linked to canopy cover although some progress has been reported using geometrical optical models, for instance Zeng et al. (2007) and Chen et al. (2012). The integration of such satellite multispectral remote sensing data with information from airborne lidar provides opportunities to capitalize upon the distinctive characteristics of both. This integration could also serve to make lidar more cost effective over larger areas (e.g., Hudak et al., 2002; Chen et al., 2012). For example, recent studies on the integration of lidar with optical remotely sensed data have focused on using lidar as a replacement for field data to extrapolate information on forest structure to landscape and regional scales (e.g., Chen et al., 2012). Models have been developed to spatially extend lidar measured attributes over larger extents using parametric approaches, which typically use multiple regression to define relationships between image spectral metrics and lidar measured tree attributes (e.g., Chen et al., 2010; Hilker et al., 2008; Hudak et al., 2002; Hyde et al., 2005). In one early study, Wulder and Seemann (2003) developed regression models to relate Landsat TM data with quantile-based estimates of canopy top height derived from SLICER (Scanning Lidar Imager of Canopies by Echo Recovery) satellite data, producing stand level mean height estimates. More recently, Pascual et al. (2010) evaluated the relationship of several Landsat-derived spectral indices with canopy height derived from airborne lidar.

Spectral indices have been demonstrated as a means to normalize and compare satellite imagery comprising a time series (Pflugmacher et al., 2012; White et al., 2011). Landsat Tasseled Cap Transformation (TCT) indices, for example, have proven reliable and robust in a range of environments (Healey et al., 2005) including the coniferous dominated conditions of coastal western North America (Song et al., 2007). To accommodate the lack of short-wave infrared bands when assembling a time series of Landsat images including both MSS and TM sensors, the Tasseled Cap Angle (TCA) was developed (Powell et al., 2010). Generally, the TCA is interpreted to be an estimate of the proportion of vegetation to nonvegetation (Powell et al., 2010; Gomez et al., 2011). Dense forest stands are expected to show higher TCA values than more open stands or bare soil (White et al., 2011).

The use of fraction images derived from spectral mixture analysis (SMA) offers a complementary approach to applying the TCA (Goodwin et al., 2005). SMA divides each pixel into its constituent materials or components using endmembers that represent the spectral characteristics of key cover types (Adams et al., 1986; Garcia-Haro et al., 1999; Smith et al., 1990, 1994). Endmembers are spectral features recognizable in an image and that constitute abstractions of real objects that can be regarded as having uniform spectral properties (Strahler et al., 1986). For example, the proportion of shadow or non-photosynthetic vegetation (NPV) would be expected to be higher in trees affected by disturbance compared to healthy (denser) tree crowns. Souza et al. (2003) indicated fraction images derived from SMA have advantages in differentiating types of disturbed forests over reflectance data or vegetation indices. Spectral mixture analysis has been used in a range of biophysical studies, for example to map the fractional abundances of photosynthetic vegetation (Elmore et al., 2000; Lobell et al., 2002) and to classify biophysical structural information (Peddle et al., 1999), and it has been used as well in numerous soil and geological applications (Asner and Heidebrecht, 2002).

In this study, our main objective was to integrate airborne lidar-derived measures of forest structure with a time series

of Landsat MSS, TM, and ETM+ TCA in areas of forest disturbance to assess if a particular stand structural and spectral condition is to result based on disturbance histories. To address the main objective, we first investigated the relationship between airborne lidar-derived forest canopy cover and Landsat-based spectral indices (with a focus on TCA) to identify the suitability of variables for use in long-term change characterization. Second, we characterized the multitemporal spectral conditions of forests that are manifested at various forest structural stages using a trajectory-based automated forest disturbance characterization method through the full temporal depth of Landsat time series. Third, we evaluated the class separability between the Landsat trajectory based disturbance classes using forest spectral and structural variability. SMA was used to assess the spectral separability of the disturbance classes as represented by spectral endmembers. Lidar-derived canopy cover was used to evaluate the disturbance class separability in terms of forest structural variability. Finally, we examined the potential of Landsat spectral indices and SMA endmembers in estimating the terminal canopy structure condition within the Landsat trajectory derived disturbance classes.

Data and methods

Study area

The study area (49°52′N, 125°20′W) is located between Courtenay and Campbell River on Vancouver Island, British Columbia, Canada (**Figure 1**). A 5.1 km × 5.1 km (2601 ha) study area corresponding to the airborne lidar data acquisition mission ranges in elevation from 120 m to

Figure 1. Study area located between Courtenay and Campbell River, Vancouver Island, British Columbia, Canada.
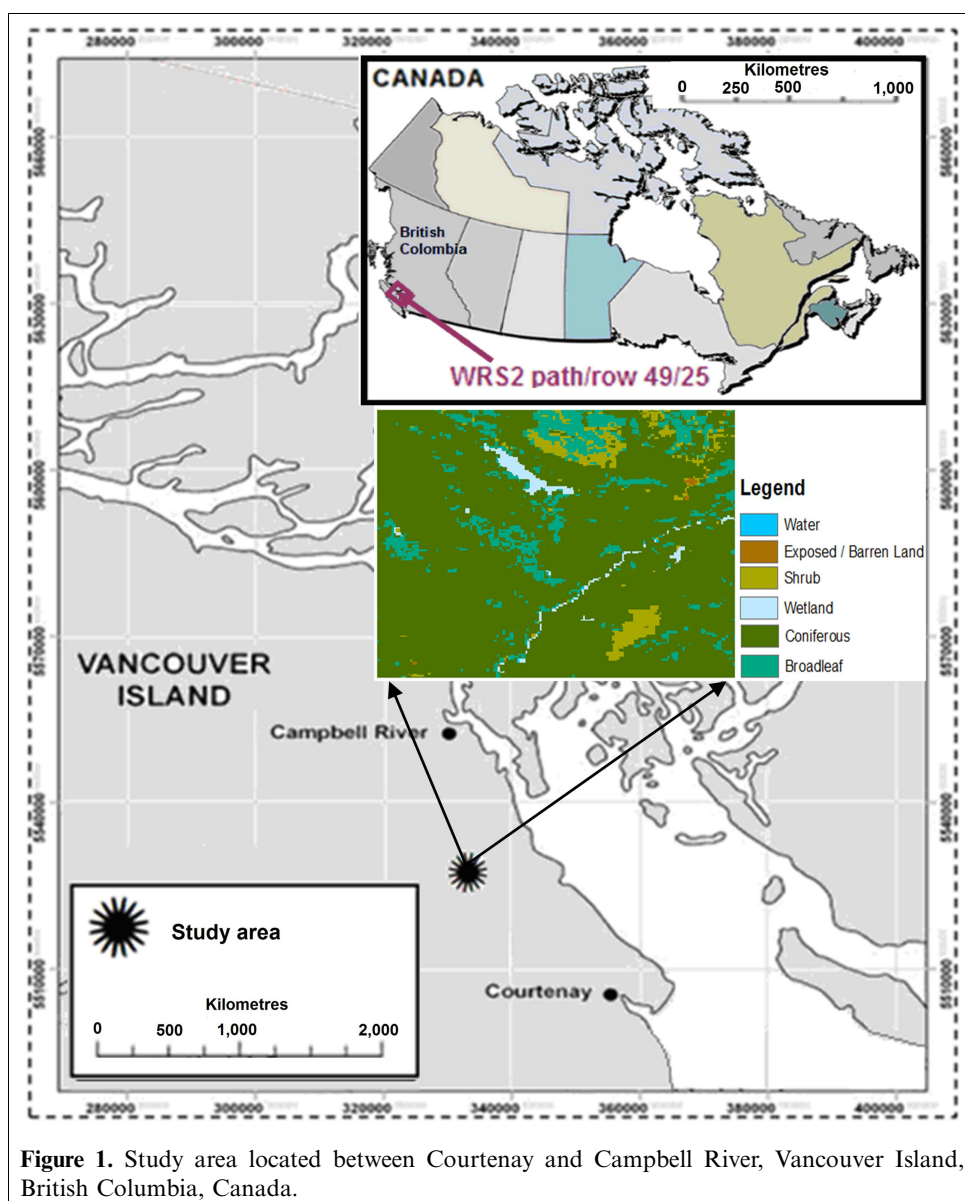
460 m, and is within 15 km of the coast. The area is characterized by mature conifer forest, regenerating conifer and deciduous stands, and harvested areas. Conifer forest types compose 65% of the study area, and are dominated by approximately 80% Douglas-fir (*Pseudotsuga menziesii* (Mirb.) Franco), with small proportions of Western Red Cedar (*Thuja plicata* (Donn.)), and Western Hemlock (*Tsuga heterophylla* (Raf.) Sarg.). Deciduous forest of Red Alder (*Alnus rubra* Bong.) comprise approximately 16% of the study area. The majority of the study area is managed by private forest companies under license. Most stands are between 20 and 60 years of age (Morgenstern et al., 2004). For mature stands, a 1998 site survey found that the stand density was approximately 1100 stems/ha.

Airborne lidar data

Discrete-return lidar data were acquired on 8 June 2004 by Terra Remote Sensing (Sidney, British Colombia, Canada) from a Bell 206 Jet Ranger helicopter. The positioning systems, a Litton LTN-92 inertial navigation system and an Ashtech Z-surveyor Dual Frequency P-code differential global positioning system, recorded the aircraft's altitude and position within 10 cm. A discrete-return lidar system (Lightwave Model 110) was used with a pulse repetition frequency of 10 kHz, a wavelength of 1047 nm, a scan angle of 56°, and a beam divergence of 3.5 mrad. Based on the pulse frequency, lowest sustainable flight speed, and altitude, hit densities of 0.7 hits/m^2 were achieved with a footprint (spot size) of 0.19 m (**Table 1**).

The raw lidar point cloud data contained both ground and nonground returns. All nonground returns are considered to be from vegetation, as no buildings or notable infrastructure are present in the study area. Classifying point cloud data into ground and tree canopy returns was implemented with Terrascan software (v4.006, Terrasolid,

Table 1. Lidar parameters.

Parameter	Performance
Sensor	Mark II
Laser scan frequency	10 Hz
Laser impulse frequency	40 000 Hz
Laser power	<4 W
Scan angle	<56°
Type of scanning mirror	Oscillating
Laser beam divergence	<0.5 mrad
Measurement decay	0.5–0.8 hits/m^2
Datum	NAD83
Projection	UTM Zone 10
Platform	Bell 206 Jet Ranger helicopter
Flight altitude above ground	900 m
Flight speed	25–30 m/s
Version of TerraScan used to classify	Version 004.006

Helsinki, Finland) which combines filtering and thresholding methods (Chen et al., 2010).

In this study, lidar-derived canopy cover (CC), was estimated using the ratio of the pulse returned from the upper layer of tree crown (sum of all pulses >1.5 m) to total returns (throughout the canopy to ground).

$$CC = \frac{\sum \text{all returns} > 1.5\,\text{m}}{\text{total returns}} \qquad (1)$$

This CC derivation method was used by several studies including Hyde et al. (2005), Morsdorf et al. (2006), Solberg et al. (2006), and Smith et al. (2009). In prior literature, the selection of the threshold above which returns are considered to be from canopy has been arbitrary. Smith et al. (2009) evaluated a selection of different height thresholds in mixed-aged forests. Their analysis determined a negligible variation in correlation (*r* difference of approx. 0.0005) between the field-densitometer-derived and lidar-derived canopy cover measures occurred when the threshold was between 1.00 and 2.00 m; therefore, for their study they selected an intermediate threshold of 1.50 m. The same threshold value of 1.50 m was used in our study to determine canopy returns. A lidar Canopy Height Model (CHM), as described in Chen et al. (2010), was used to derive tree heights for use in statistical modeling and in the spectral mixture analysis. The CHM was derived by separately interpolating the classified ground and tree canopy returns (Hutchinson, 1989) to form a digital elevation model (DEM) and a digital surface model (DSM) with 1 m grid cell size. The final step was to obtain the CHM by subtracting the DEM from the DSM. To match the spatial resolution of the Landsat imagery, the final lidar-derived estimates of canopy height were resampled from 1 m to 30 m resolution using simple averaging.

Landsat data

The Landsat imagery for the study area was obtained from the United States Geological Survey (USGS) Landsat archive. We used a combination of MSS, TM, and ETM+ imagery. All of the MSS, TM, and ETM+ data were system-corrected for terrain and were converted to "top-of-atmosphere-radiance" (L1T data product). The study area falls within WRS2 path–row 49–25, and a time sequence of 16 Landsat images from (1972–2004) was available for this area (**Table 2**). All images were selected within the summer and early fall seasons for consistency in forest phenological condition (Wulder et al., 2004).

Landsat image preprocessing

Based on image quality and cloud-free status, the 1989 TM image was selected as the reference image (**Table 1**). We coregistered all MSS and ETM+ imagery to the reference TM image using an automated registration and orthorectification

Table 2. Available Landsat time-series of imagery.

Year	Available Landsat (yyyy-mm-dd)	Path	Row	Sensor
1972	1972-08-19	53	25	MSS
1974	1974-08-09	53	25	MSS
1984	1984-09-26	49	25	TM5
1985	1985-09-06	49	25	TM5
1989	1989-08-07	49	25	TM5
1990	1990-08-10	49	25	TM5
1991	1991-08-13	49	25	TM5
1992	1992-08-15	49	25	TM5
1993	1993-09-03	49	25	TM5
1995	1995-06-05	49	25	TM5
1997	1997-08-13	49	25	TM5
1998	1998-06-13	49	25	TM5
1999	1999-09-12	49	25	ETM +
2000	2000-08-13	49	25	ETM +
2002	2002-08-27	49	25	TM5
2004	2004-08-16	49	25	TM5

package (Gao et al., 2009). To match the spatial resolution of the TM and ETM+ data, we resampled the MSS imagery to 30 m. Coregistration was performed on the entire scene overlap. Images with a final root mean square error (RMSE) in the coregistration greater than 0.5 pixels were removed from the analysis.

To minimize annual variations in atmospheric conditions, we normalized each image in the Landsat time series to the 1989 TM reference image located in the middle of the series. First, the cosine estimation of atmospheric transmittance absolute radiometric correction model of Chavez (1996) was applied to the reference image to convert digital counts to surface reflectance. This model consists of a modification of the dark-object subtraction method by including a simple multiplicative correction for the effect of atmospheric transmittance.

Following Schroeder et al. (2006), all other TM and ETM+ images in the time series were radiometrically normalized to the reference image using the multivariate alteration detection and calibration algorithm (MADCAL) of Canty et al. (2004). This automatic process identifies invariant pixels between image pairs and performs a relative normalization using orthogonal regression of the target image pixels on to the reference image pixels. The process of normalization reduces artifacts due to illumination or atmospheric variations, enabling more reliable detection of true change (Song et al., 2001). Water, clouds, and cloud shadows were masked using an object-based cloud and cloud shadow detection algorithm for Landsat imagery (Zhu et al., 2011). This approach uses various bands of Landsat data converted to top-of-atmosphere reflectance and brightness temperature and cloud physical properties to separate cloud pixels and clear sky pixels, and then produces separate masks for clouds, cloud shadows, and water.

Tasseled cap transformation (TCT)

To assemble time series relating conditions from 1972 to 2004 it was required to integrate data from multiple Landsat sensors, including MSS, TM, and ETM+ sensors. The image normalization process, in the previous section, creates a spectral space that is relatively consistent across sensors. A single spectral transformation, the TCT (Crist, 1985; Huang et al., 2002), was used for all Landsat images in the time series. TCT is a well-known linear transformation widely employed (Cohen and Goward, 2004) to characterize forest structure (Cohen et al., 2002; Hansen et al., 2001), condition (Healey et al., 2006; Wulder et al., 2006), and in change detection (Jin and Sader, 2005).

The first TCT component corresponds to the overall "brightness" of the image and, by definition, is a positive value. The second TCT component corresponds to "greenness" and is typically used as an indicator of the amount of photosynthetically active vegetation. The values for greenness depend on the contrast between the visible and near-infrared bands, with exposed soil having negative values (Gillanders et al., 2008) and vegetated areas having positive values. The third TCT component is often labeled "wetness" and is usually interpreted in vegetated areas as an index of canopy structure, soil or surface moisture, or possibly an estimate of the amount of dead or dried vegetation (Cohen and Goward, 2004). Brightness and greenness define the vegetation plane (Crist and Cicone, 1984) and provide a practical bridge between the earlier MSS imagery and more recent TM and ETM+ imagery (Powell et al., 2008).

Structural differences in forest vegetation have been most effectively described with indices that utilize the contrast between short-wave and near-infrared reflectance, such as wetness (Cohen and Goward, 2004). However, MSS sensors lack short-wave infrared bands, and therefore wetness cannot be computed for Landsat MSS imagery. Alternatively, an index called TCA, defined by Powell et al (2010), has been developed as the angle formed by brightness and greenness in the vegetation plane (Equation (2)). TCA has been interpreted as an indicator of the proportion of vegetation to non-vegetation within a Landsat MSS, ETM+, or TM pixel (Powell et al., 2010; Gomez et al., 2011):

$$TCA = \arctan (greenness / brightness) \qquad (2)$$

Higher values of greenness and lower values of brightness are often found over forests, and therefore, higher values of TCA are more likely in dense cover classes when compared with open stands or clearcuts (Cohen et al., 1998; Price and Jakubauskas, 1998; White et al., 2011). TCA was used to describe change in the present study, although we also used the original TCT values and other indices such as Normalized Difference Vegetation Index (NDVI), for available Landsat imagery in later statistical modeling. Another TCT derivative called Tasseled Cap Distance (TCD), used

by Duane et al. (2010) to predict forest age, was also included in the current analysis for comparison.

$$TCD = \sqrt{(TCG^2 + TCB^2)} \qquad (3)$$

The water, cloud, and cloud shadow pixels were masked and excluded from this study. The remaining Landsat pixels were transformed using the appropriate TCT coefficients for reflectance data (e.g., Crist, 1985). For the Landsat MSS TCT, we used the coefficients presented by Pflugmacher et al. (2011). Recently, the USGS-Earth Resources Observation and Science (EROS) switched the processing of the MSS archive to LPGS (Level 1 Product Generation System) resulting in new post-calibration dynamic ranges and data quantization that are significantly different from the ones previously used. Because the MSS TCT is a digital number (DN) based transformation, it is affected by the post-calibration coefficients used to rescale the calibrated radiance data to calibrated DN.

To normalize MSS data with the TM and ETM+ time series we used the available TCT components with MADCAL rather than the individual spectral bands (Powell et al., 2008). The brightness and greenness components derived from the 1989 Landsat TM image were used as the reference source for MADCAL. The MADCAL process has

been shown to be invariant to linear transformations (Canty et al., 2004).

Fitting of spectral trajectories

An automated curve-fitting algorithm was used to characterize change in TCA over the available 32-year Landsat time series (1972–2004). After the final set of best predictor models were identified and the results compared, the Landsat time series was arranged for spectral trajectory fitting. As our preliminary tests indicated high correlation between TCA and lidar-derived canopy cover, TCA was used as a proxy of canopy cover to characterize change through the full temporal depth of the Landsat dataset.

The same curve-fitting algorithm was used by Kennedy et al. (2007) and requires no specific threshold development. In our study, the curve fitting parameters were altered from Kennedy et al. (2007) in order to capture the distinctive characteristics of TCA.

In addition to "stable and undisturbed forest", we identified four classes of potential temporal trajectories of change in TCA: Class 1, disturbance; Class 2, disturbance followed by revegetation; Class 3, ongoing revegetation; and Class 4, revegetation to a stable state (**Figure 2**). These four
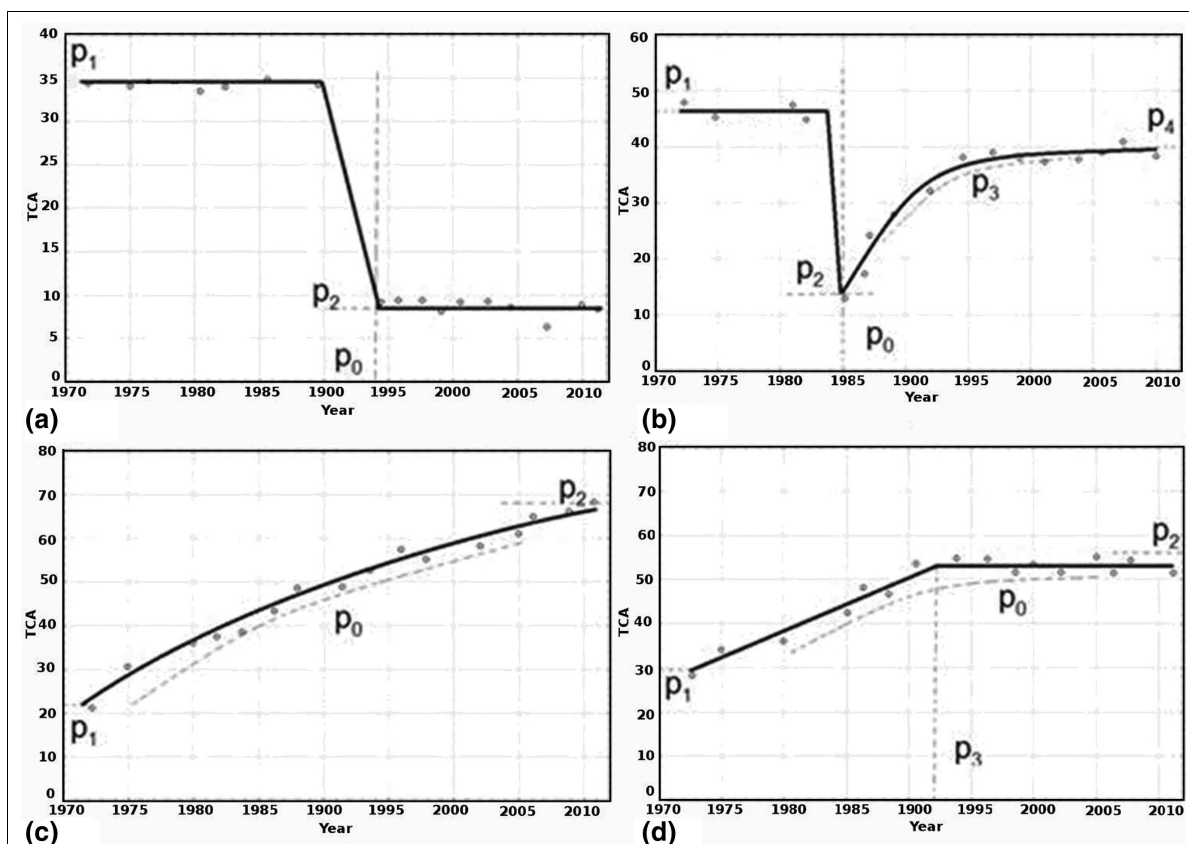

Figure 2. Example of the four disturbance class spectral trajectories and parameters fit to each trajectory. Tasseled Cap Angle (TCA) scaled by 100. (a) Disturbance, (b) disturbance followed by revegetation, (c) ongoing revegetation, and (d) revegetation to a stable state.

disturbance classes are used throughout this paper. Our interpretation of the spectral characteristics of these classes was similar to Gomez et al. (2011), who found that dense forest stands had higher TCA values than more open stands or bare soil, and that TCA values in recent clearcuts were significantly lower than in any other stage of stand development. Generally, TCA displays an increasing trend with time since disturbance.

We extracted TCA for each pixel in the Landsat time series (1972–2004). For each of the four classes (**Figure 2**) we created initial estimates of spectral trajectory shape parameters and then used a fitting function to adjust these initial parameters to find the best fit of the potential trajectory to the observed trajectory. The fitting algorithm calculates the standard f statistic, and the probability of that f statistic p value occurring between the potential classes and the observed TCA trajectories. The model with the lowest p value was selected as a best model for each pixel in the final output image. In this process, pixels without change could result in high p values even for that best model (Kennedy et al., 2007). Therefore, no-change pixels were identified as those pixels where the best model had a p value higher than 0.05. The parameters describing the best model were input to a separate layer of the output image.

After identifying the four classes of spectral trajectories, we developed appropriate functions to describe these patterns. In our interpretation, the parameters describing those functions capture the key characteristics of disturbance and regrowth. For example, disturbance through partial and clearcut harvest typically results in a step function in TCA (**Figure 2a**). When a forest stand is removed through disturbance, TCA declines quickly from an initially high value to a low value, and in the absence of subsequent revegetation, remains low. The parameter values describing this spectral trajectory shape are the end year of the disturbance interval (parameter p_0), the pre-disturbance mean TCA (p_1), and the post-disturbance mean (p_2).

When disturbance is followed by revegetation, TCA initially declines, but then increases over time (**Figure 2b**). The trajectory from low to high TCA in this class is expected to follow an exponential curve. Two parameters describing this trajectory are identical to those in the first disturbance class: the pre-disturbance mean TCA (p_1) and the year after disturbance (p_0). Parameters p_2, p_3, and p_4 describe the exponential function that captures the return of TCA to higher value. The exponential function is:

$$\text{TCA} = ((p_4 - p_2)(1 - e^{-p_3^t})) + p_4 \qquad (4)$$

where TCA is the observed TCA, p_3 is an exponential constant, p_2 and p_4 are lower and upper bounds, respectively, on the exponential function, and t is the time since disturbance (in years). The parameter p_2 is analogous to the mean TCA value immediately after disturbance in the previous disturbance function, whereas the parameter p_4 describes the asymptotic level of TCA if the exponential function were to continue to infinity. The parameter p_3

describes the rate of increase in TCA from the low value p_2 to a value at p_4. Higher value of p_3 indicates faster recovery of vegetation. Because TCA represents a proportion, the exponential parameter was constrained to a range from 0 to 1.

The third potential trajectory (ongoing revegetation followed by recovery from disturbance) is represented by exponential recovery alone, without an observed disturbance event (Equation (4)). In this trajectory t represents the time since the beginning of the record, and p_2 represents the TCA value for the first year of the record.

The fourth trajectory (represented by Class 4, revegetation to a steady state) uses the same equation as Class 3 (ongoing revegetation trajectory), but assumes that the TCA value stabilizes to an unchanging constant at some point before the time series ends. Consequently, one additional parameter is added to the function that corresponds to the year at which a stable TCA was reached.

After defining the parameters for the four disturbance class trajectories, a least-squares curve of each potential trajectory was fitted to the observed TCA trajectory in each pixel. For this curve fitting we used MPFIT Markwardt (2008), which is a Non-Linear Least Squares Fitting algorithm adapted for IDL (Interactive Data Language, ITT Visual Information Solutions, Inc.). This procedure allows the user to develop functions of any arbitrary form that define how a set of arbitrary parameters converts a set of X values into a set of Y values (Kennedy et al., 2007). Initial estimates of parameter values are sent to MPFIT, and then the program returns the adjusted parameter set that best fits the observed trajectory.

Initial estimates of the required parameters were set for the four potential trajectories. For the first two disturbance trajectory classes, the year of disturbance was fixed at the point where the decline in TCA from one year to the next was greatest. Estimates of pre- and post-disturbance TCA values were taken as arithmetic means of TCA in the years before and after the estimated year of disturbance. For the other trajectory classes involving exponential increases, the initial estimate of the constant was calculated as the difference of the log of the TCA immediately after disturbance (or at the beginning of the record for ongoing revegetation and the revegetation to stability types) and the log of the TCA in the following year. When this value was less than or equal to zero, an initial estimate of zero was used. Bounding constraints of the exponential functions were TCA value at the year of disturbance (p_2) and zero (p_1). For the "revegetation to stability" class, initial estimates of stability level and onset of stability were estimated as the TCA value at the end of the record and the last year of the record, respectively.

The four classes are considered competing models for the observed conditions. Standard f statistic and the probability of that f statistic (p value) were calculated between the potential class and the observed trajectories in each pixel and the model that had the lowest p value was selected to

represent the trajectory in that specific pixel. The parameters of the best model fully describe the disturbance and recovery dynamics for the pixel and are then written as a separate layer in the output image. The model parameters written to the output image describe important aspects of the disturbance regime, including year of disturbance. The temporal curve-fitting was applied to the time series of Landsat-based TCA values listed in **Table 2**. The method is extremely computer intensive, taking weeks to process a single stack of the time series for the area of one Landsat scene. For the purposes of this study, we constrained the analysis only to the portion of the study area overlapping with the airborne lidar data.

Validation of the trajectory characterization

Validation of change-detection maps derived using satellite observations typically relies on independent reference data collected through ground-based field work, visual interpretation of high resolution images, or both (Congalton, 1991; Stehman and Czaplewski, 1998). For the disturbance information derived in this study, however, such a validation approach is inapplicable as changes must be validated for near-yearly periods spanning four decades. In this study, because no suitable independent datasets were available for every year of the record for the entire area, we used a complementary approach to assess the performance of the outputs from the trajectory-based method using visual interpretation of the imagery itself (Cohen et al., 1998; Kennedy et al., 2007; Masek et al., 2008; Huang et al., 2009). Cohen et al. (1998) showed that direct human interpretation of tasseled-cap transformed Landsat imagery was as accurate for mapping forest clear-cuts as both independent photo and field-based datasets, even though the imagery used for interpretation was the same source used to make the change-detection map. In this study, the disturbance classes derived through trajectory-based method were not directly validated because the visual interpretation approach can not provide definitive validation information on the temporal curve fitting derived disturbance classes. However, the change–no-change areas and disturbance year, which comprise the key parameters for the trajectory-based method to construct the disturbance classes, can be reliably identified and validated by a comparison between the pre- and post-disturbance Landsat images. Because of the intensive effort required, we used this approach to validate a relatively small number of validation sites. Within the areas labeled as disturbed forest by the algorithm (i.e., combining the classes: disturbance and disturbance followed by revegetation), a total of 150 validation points were selected using a stratified random sampling approach. Specifically, the disturbance year map was used to define the strata where each class was a stratum. The number of points selected from each stratum was proportionate to its areal extent within the image with a constraint that the validation points were no closer than

three pixels from the existing sample, to limit the effects of spatial autocorrelation among samples. In addition, if a validation sample was located on an edge of a disturbance year polygon as determined through visual inspection, the validation sample was relocated within three pixels from the original location to avoid confusion caused by any misregistration. These 150 samples were used to evaluate the performance of the trajectory-based method in capturing the actual disturbance year, which constitutes one of the key parameters (p_0) describing the trajectory for the classes disturbance and disturbance followed by revegetation (**Figures 2a** and **2b**). Each of the 150 disturbed sample points were attributed with disturbance year. A similar process was applied to the areas labeled as stable forest by the algorithm, inferred to be "no-change" resulting in additional 150 randomly selected no-change samples obtained without any stratification using the abovementioned sampling constraints. Because it was impossible to know when the disturbances occurred in the ongoing revegetation and revegetation to a stable state classes that were identified by the trajectory-based method, an additional 100 random samples were selected from these two classes to evaluate the performance of the trajectory-based method in capturing pre-observation disturbance (pixels that were disturbed before the first image acquisition). The pre-observation disturbance constitutes one of the key parameters (p_1) in the ongoing revegetation and revegetation to stable state, disturbance class trajectories (**Figures 2c** and **2d**). The total 400 samples of no-change, disturbance year, and pre-observation disturbance were then compared with visual interpretation to determine the appropriate no-change, disturbance year, and pre-observation disturbance label. The Landsat images were inspected in sequence from the earliest to most recent data in ArcMap to determine whether and when disturbances occurred at each sample location. Year-to-year difference images were used as an initial visual guide for identifying potential disturbance, but the final interpretation of the disturbed area was based on the original TCA imagery. Finally, a sample was labeled "correct" if the pixels in the visual interpretation were labeled the same in the algorithm-derived image. Errors were tabulated for the labels no-change, year of disturbance, and for pre-observation disturbance. Standard error matrix and summary statistics were then calculated (Congalton and Green, 1999).

Extraction of disturbance class spectral characteristics

After characterizing the multitemporal spectral conditions of forests using the trajectory-based disturbance characterization method it was found prudent to assess the class separability between the identified disturbance classes in terms of both forest spectral and structural variability. In this study, SMA was selected to derive spectral characteristics for the Landsat trajectory based disturbance classes to assess the class separability as represented by spectral endmembers. SMA was ideal for this study as it

recognizes the spatially heterogeneous mixtures of vegetation, soil, shadow, and others in forest canopies rather than a single cover type. In contrast to using other vegetation indices, SMA endmembers describe a physical property of the landscape and lend themselves to straightforward interpretation based on the available disturbance information. Souza et al. (2003) indicated fraction images derived from SMA have more advantages in differentiating types of disturbed forests than reflectance data and vegetation and infrared indices. In this study, SMA was used to derive spectral characteristics for the four disturbance classes in the Landsat trajectory. Using the 2004 Landsat TM imagery we generated sub-pixel fraction images for the Landsat-derived forest disturbance classes (as identified in the previous section). Lu et al. (2004) demonstrated that the removal of highly correlated bands such as TM 1 and TM 2 in SMA improves the quality of fraction images. Thus, in this study to reduce correlation and data redundancy we used Landsat TM band subset images (i.e., bands 3, 4, 5, and 7) in the SMA.

An important prerequisite to successful SMA is the selection of representative endmembers (Somers et al., 2011; Tompkins et al., 1997). Here endmembers representing sunlit canopy, NPV, exposed soil, and shade were derived from the Landsat multispectral image using the n-dimensional visualization tool (available in ENVI 4.8) and the lidar data. The variation in understory reflectance that can be present within a typical Landsat pixel can cause difficulties in SMA endmember selection. This variation in understorey reflectance is manifest within individual pixels and across a given scene. In this study, to reduce the influence of understory vegetation on SMA fractions, tree height information derived from lidar was used to help guide the selection of endmembers. For example, tree height information derived from lidar aided in the selection of NPV and exposed soil endmembers by identifying sites with low or no vegetation cover using a canopy height threshold of 1.50 m. The pixels located at the extremes of the data cloud of the Landsat spectral space in the n-dimensional visualization tool were selected as candidate endmembers. The final endmembers were selected based on the spectral shape and image context (e.g., soil spectra are mostly associated with unpaved roads and NPV with understory grass having senesced vegetation).

We applied least-square linear mixture modeling (Adams et al., 1993) to estimate the proportion of each endmember within the Landsat pixels. The sums of the fractions add up to 1. The n-dimensional visualisation tool was also used to check the separability of the endmembers and refine the selected regions of interest. The SMA model results were evaluated (Adams et al., 1995) with the root–mean–square image and fraction images interpreted in terms of image context and spatial distribution.

Finally the fractions were summarized within each trajectory-derived disturbance class to obtain mean values for each class. This allowed the extraction of the spectral characteristics for each disturbance class and quantified the fractional abundances of the key image endmembers (sunlit canopy, NPV, bare soil, and shade) within each class to assess the class separability between disturbance classes as represented by spectral endmembers. We used a Tukey test (Ott, 1992), available in the R Language (http://www.r-project.org/) to evaluate if the disturbance classes could be separated from each other. This test was run at a 99% confidence interval ($p < 0.01$). For the purpose of the class separability, the Tukey test performs a multicomparison of the population means of the disturbance classes; that is, it tests the mean of a population against the mean of each other population. Further, as the test requires normally distributed samples, a data transformation was applied when necessary.

Relationships between disturbance class spectral characteristics and lidar forest structural measurements

In the final step of the analysis, we explored how Landsat spectral trajectories related to the terminal forest structural conditions that were found in the lidar data and as a function of disturbance history. The terminal canopy structure attributes (related by canopy cover and height) were extracted from the lidar data within each disturbance class to determine the structural variability between disturbance classes. The uniqueness of the structural conditions by disturbance class was tested using analysis of variance.

To compare the potential of Landsat spectral indices and SMA fraction images in estimating canopy structure within disturbance classes and to test their estimation advantage, multiple regression analysis was conducted to assess the relative importance of each independent variable in explaining the lidar-derived canopy cover and height. The input variables were extracted using stratified random sampling based on disturbance classes. For the dependent and independent variables random data subsets were created for modeling and a second subset for validation, which was used to assess the prediction accuracy. The samples were selected proportional to the areal coverage of each disturbance class, as it was expected that they would sufficiently represent the distribution of crown cover and height of each class. To better describe forest structure within disturbance classes, separate regression models were developed for each disturbance class. First a check of the multicollinearity between predictor variables in the regression analysis was carried out among the independent variables. Landsat spectral indices and SMA fractions with high correlation among each other were excluded in this regression analysis. For all the combinations, each independent variable was evaluated and retained if its correlation value with any other independent variable was lower than 0.7. A stepwise variable selection method, used by Wulder et al. (2004), was adopted

in this study to determine the most significant input variables for modeling.

Statistical treatment was performed with the Statistica program version 10. Before proceeding with the analysis, the necessary transformations (i.e., logarithm and inversion of variables) were made to adjust the distributions of variables to the prerequisites required for the regression analysis. Normality was checked using the Shapiro–Wilks test.

Finally, an independent validation served as a basis for comparing the performance of Landsat spectral indices and SMA endmembers in estimating disturbance class canopy structure. The models were assessed using RMSE and the predictions were evaluated against the validation dataset, R^2 and the RMSE are reported. The flowchart in **Figure 3** summarizes the overall approach of this study described in the preceding subsections.

Results

Airborne lidar-derived canopy cover estimates and Landsat-derived spectral transformations and indices for the study are depicted graphically (**Figure 4**), with the uniqueness of the indices being visually apparent. A strong and significant correlation coefficient was obtained for TCA ($r = 0.86$), with lower though still significant correlations between lidar-derived canopy cover with NDVI ($r = 0.62$) and greenness ($r = 0.37$) (**Table 3**). The weakest correlation coefficient was obtained using the brightness component.

Trajectory-based characterization of forest disturbance

Because our tests, which are outlined above, indicated high correlation between TCA and lidar-derived canopy cover,
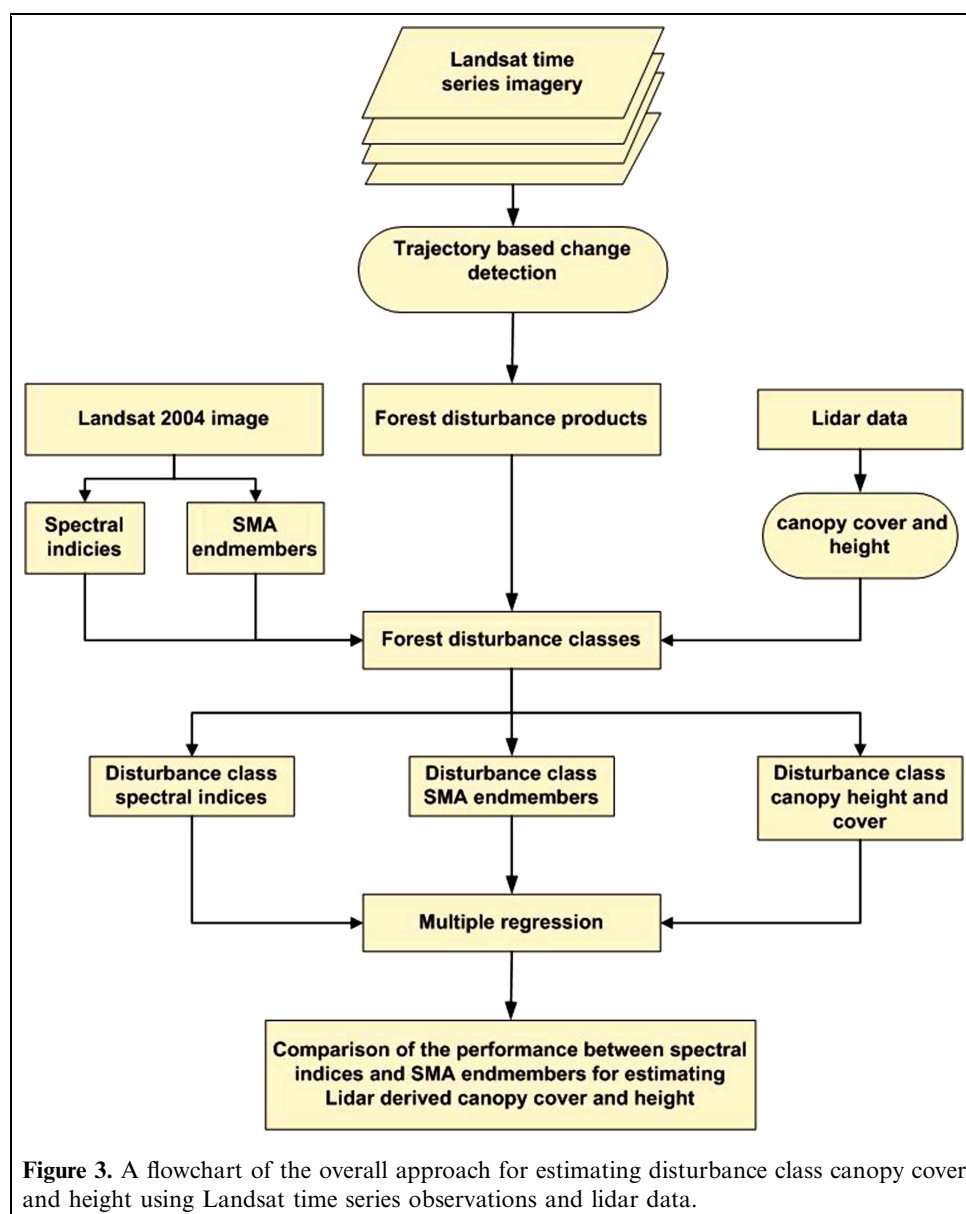

Figure 3. A flowchart of the overall approach for estimating disturbance class canopy cover and height using Landsat time series observations and lidar data.
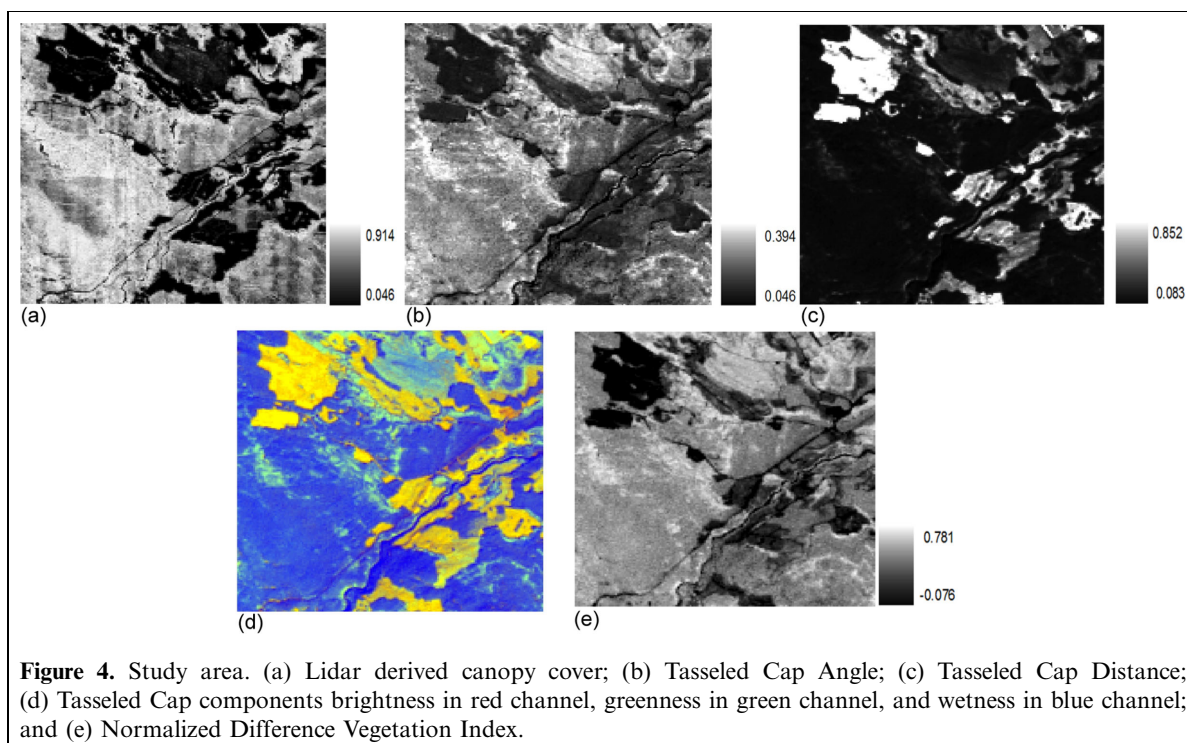
Figure 4. Study area. (a) Lidar derived canopy cover; (b) Tasseled Cap Angle; (c) Tasseled Cap Distance; (d) Tasseled Cap components brightness in red channel, greenness in green channel, and wetness in blue channel; and (e) Normalized Difference Vegetation Index.

TCA was used as a proxy to canopy cover to characterize change, this supported the development of forest disturbance products through the full temporal depth of the Landsat time series in the study area. The curve fitting process resulted in an output image with the attributes corresponding to the fitting parameters for each pixel whose trajectory matched one of the four potential trajectories in the disturbance classes at the p value ≤ 0.05. The fitted potential trajectories for the study area are shown in **Figure 5**. The results indicated that from 1972–2004, approximately 71.5% of the study area showed "stable and undisturbed forest" structure. The areas characterized by disturbance account for 10.19%, disturbance and revegetation 5.25%, ongoing revegetation 2.19%, and revegetation to stable state account 10.15% of the study area.
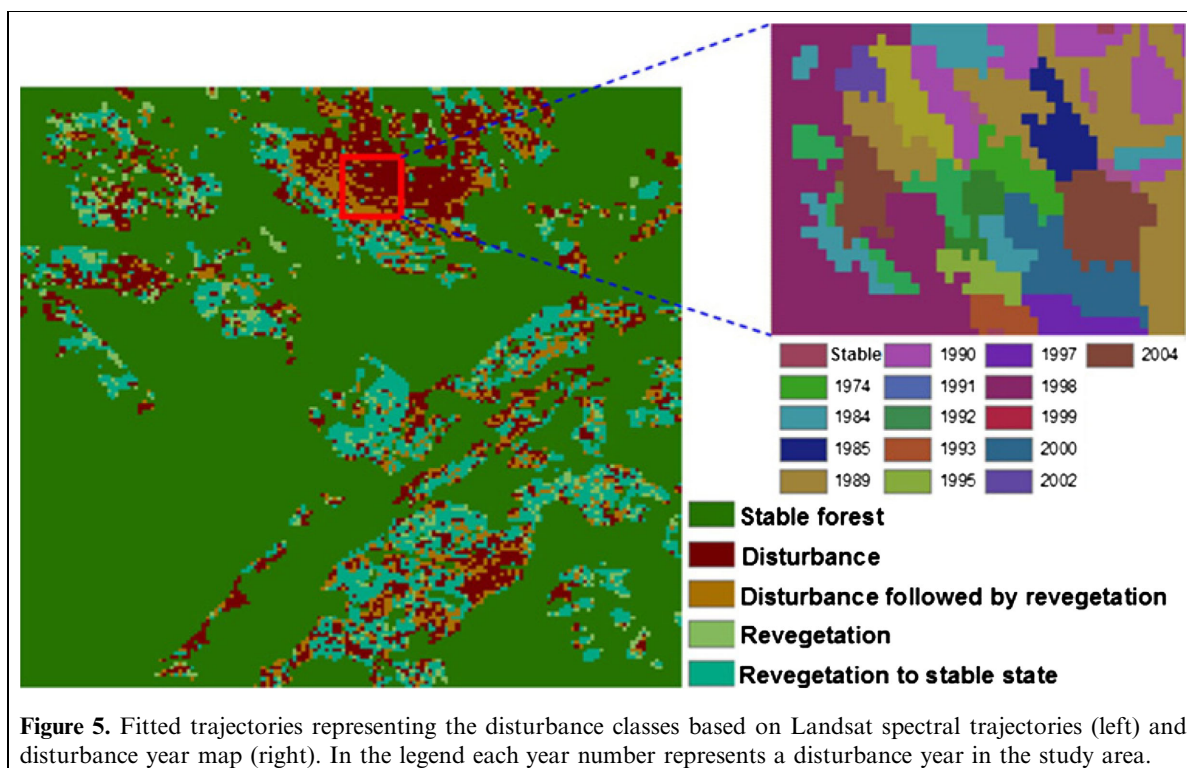
Accuracy assessment

The trajectory-based algorithm derived stable (no-change) areas, disturbance year, and pre-observation disturbance for the randomly selected 400 points were validated using the approach described in "Validation of the trajectory characterization". The overall user's and producer's accuracies were calculated according to Congalton and Green (1999). At per-pixel level the overall accuracy was 82.8% (**Table 4**). All the points had relatively high user's accuracy values. Whereas the lowest user's accuracies were just over 63%, the majority of the disturbance years had user's accuracies of over 70%. The average user's and producer's accuracies were 75.2% and 68.8%, respectively.

The confusion matrix reveals distinctive patterns of errors by the trajectory-based algorithm. The algorithm missed a

Table 3. Correlation coefficients between Landsat spectral indices and lidar canopy cover.

	TCA	TCD	TCW	B5R	TCG	TCB	NDVI	Canopy cover
TCA	1.0	0.04	0.22	−0.05	0.66	0.06	0.58	0.86
TCD	0.04	1.0	−0.90	0.93	0.71	0.93	0.13	0.08
TCW	0.22	−0.90	1.0	−0.97	−0.55	−0.95	0.12	0.16
B5R	−0.05	0.93	−0.97	1.0	0.69	0.98	−0.02	−0.04
TCG	0.66	0.71	−0.55	0.69	1.0	0.77	0.37	0.37
TCB	0.06	0.93	−0.95	0.98	0.77	1.0	0.02	−0.002
NDVI	0.58	0.13	0.12	−0.02	0.37	0.02	1.0	0.62
Canopy cover	0.86	0.08	0.16	−0.04	0.37	−0.002	0.62	1.0

Note: TCA, Tasseled Cap Angle; TCD, Tasseled Cap Distance; TCW, Tasseled Cap Wetness; B5R, band 5 spectral response data; TCG, Tasseled Cap Greenness; TCB, Tasseled Cap Brightness; NDVI, Normalized Difference Vegetation Index.

Figure 5. Fitted trajectories representing the disturbance classes based on Landsat spectral trajectories (left) and disturbance year map (right). In the legend each year number represents a disturbance year in the study area.

significant amount of changes and labeled them as no-change (stable) forest instead. In total 24 such samples were mislabeled. The majority of those changes (19 of 24), however, were identified as minor changes by the interpreter. Because of the lack of ground information or high resolution data collected immediately after the occurrence of each disturbance, here the distinction between major and minor disturbances was determined by visually checking the post-disturbance Landsat images. After a minor disturbance, the post-disturbance pixels are brighter and less green than the pre-disturbance pixels; but they still looked similar to forest pixels. For a major disturbance caused by clear cut or other stand replacing events, however, the post-disturbance pixels looked completely different from forest pixels.

Most of the errors located below the diagonal of the confusion matrix (**Table 4**), indicate that many early-year disturbances in the visual interpretation were mapped as disturbances in later years by the trajectory-based algorithm. Examination of the 20 points that had this problem indicated that 13 of the points had a minor disturbance in an early year followed by a major disturbance in a later year, which was detected correctly by the algorithm. This indicates, in spite of the errors below the diagonal in **Table 4**, the majority of the changes mapped by the algorithm were disturbances that had actually occurred.

Disturbance class separability

The fraction images derived from the SMA provided useful information on the disturbance classes spectral characteristics (i.e., disturbance, disturbance followed by revegetation, ongoing revegetation, and revegetation to a stable state; **Figures 6** and **7** in the study area). The images show clear differentiation in abundances between sunlit canopy, NPV, shade, and exposed soil. NPV and shade fractions were higher in the disturbance and disturbance followed by revegetation classes, with lower vegetation content (**Figure 7**).

The class disturbance, followed by revegetation, showed the highest NPV fraction values (mean = 13%), whereas ongoing revegetation and revegetation to stable state classes had similar NPV mean values (mean = 3.9% and 3.2%, respectively (**Figure 7**)). The main difference between the ongoing revegetation class and disturbance followed by revegetation class is in the sunlit canopy fraction. The ongoing revegetation class showed a lower shade fraction (mean = 38.3%) content than the disturbance followed by revegetation classes (mean = 56.6%).

The ongoing revegetation class resulted in a lower shade fraction (mean = 38.3%) and higher sunlit canopy (mean = 56.4%) when compared with stable forest. This ongoing revegetation class generally includes the earliest disturbed forest areas undergoing regeneration. The shade fraction values are typically high across all successional stages (**Figure 7**).

Table 5 shows the fraction statistics for disturbance, disturbance followed by revegetation, ongoing revegetation, and revegetation to a stable state, as represented by the stable forest class. Means with the same superscript letters showed no significant statistical differences (Tukey test, $p <$ 0.01), whereas different superscript letters indicate difference

Table 4. Confusion matrix for interpreted and algorithm-derived labeling of disturbance year and pre-observation disturbance.

							Interpreted												
Algorithm	NC	P-OD	1974	1984	1985	1989	1990	1991	1992	1993	1995	1997	1998	1999	2000	2002	2004	Row total	User's accuracy (%)
NC	**137**	6	2	2	1	3	0	1	0	1	0	1	1	2	1	2	1	161	85.09
P-OD	1	**86**	1	0	0	0	0	0	0	0	0	0	0	0	0	0	0	88	97.73
1974	1	3	**7**	0	0	0	0	0	0	0	0	0	0	0	0	0	0	11	63.64
1984	2	0	0	**11**	0	1	0	0	0	0	0	0	0	0	0	0	0	14	78.57
1985	0	0	0	0	**6**	0	0	0	1	0	0	0	0	0	0	0	0	7	85.71
1989	0	2	0	0	1	**7**	0	0	0	0	0	0	0	0	0	0	0	10	70.00
1990	1	0	0	0	1	0	**8**	0	0	0	0	0	0	0	0	0	0	10	80.00
1991	0	0	0	0	0	0	1	**5**	0	0	0	0	0	0	0	0	0	6	83.33
1992	1	0	0	1	0	0	1	0	**7**	0	0	0	0	0	0	0	0	10	70.00
1993	2	1	0	0	0	0	0	1	1	**9**	0	0	0	0	0	0	0	14	64.29
1995	0	0	0	0	0	1	0	0	0	0	**5**	0	0	0	0	0	0	6	83.33
1997	0	2	0	0	0	0	0	0	0	0	0	**5**	0	0	0	0	0	7	71.43
1998	3	0	0	0	0	0	0	0	0	0	1	2	**13**	0	0	0	0	19	68.42
1999	1	0	0	0	0	0	0	0	0	0	0	1	1	**6**	0	0	0	9	66.67
2000	0	0	0	0	0	0	0	0	0	0	1	0	1	2	**8**	0	0	12	66.67
2002	0	0	0	0	0	0	0	1	0	0	0	0	0	0	0	**4**	0	5	80.00
2004	1	0	0	0	0	0	0	1	1	0	0	0	0	0	1	1	**7**	11	63.64
Column total	150	100	10	14	9	12	10	9	9	10	7	9	16	10	10	7	8	400	
Producer's accuracy (%)	91.33	86.00	70.00	78.57	66.67	58.33	80.00	55.56	0.78	90.00	71.43	55.56	81.25	60.00	80.00	57.14	87.50		

Note: The overall accuracy is 82.8%, per class agreements are in bold face. Class codes are NC, no change; P-OD, pre-observation disturbance.
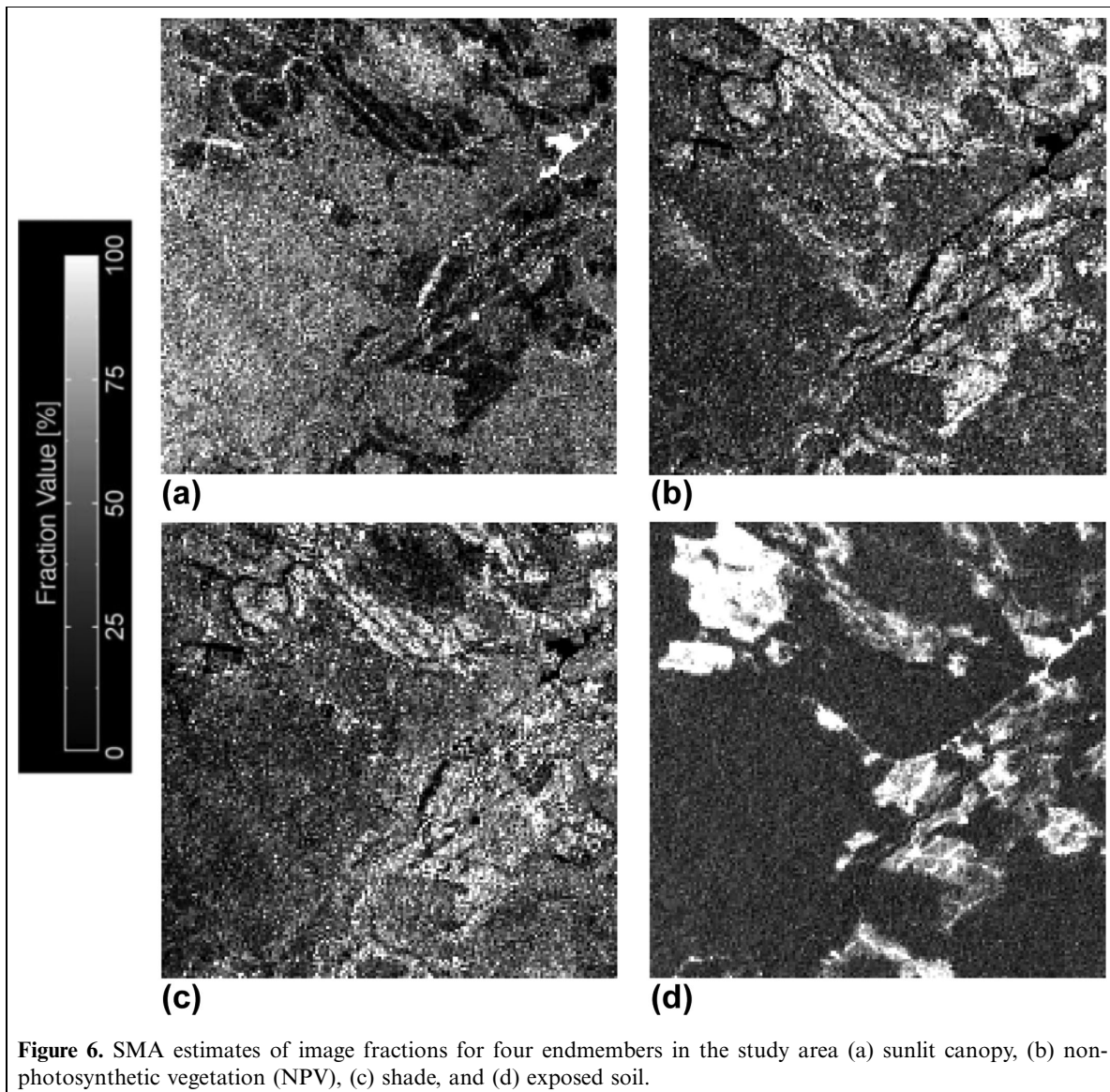
Figure 6. SMA estimates of image fractions for four endmembers in the study area (a) sunlit canopy, (b) non-photosynthetic vegetation (NPV), (c) shade, and (d) exposed soil.
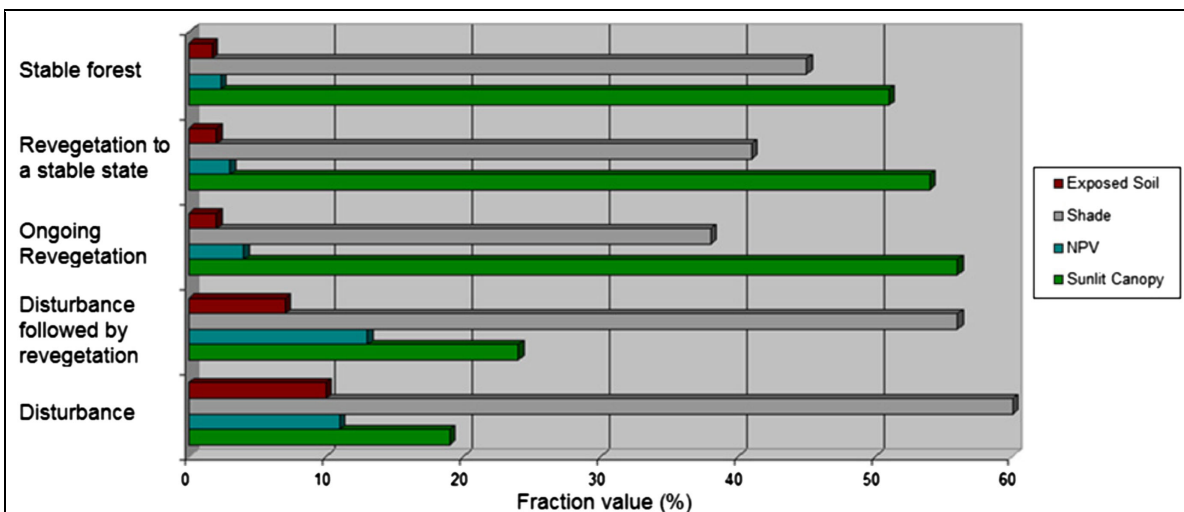

Figure 7. Mean values of fraction images summarized within disturbance classes.

Table 5. Means and standard deviations for forest disturbance classes.

Class	Disturbance		Disturbance followed by revegetation		Ongoing revegetation		Revegetation to a stable state		Stable forest	
	Mean	Standard deviation	Mean	Standard deviation	Mean	Standard deviation	Mean	Standard deviation	Mean	Standard deviation
Sunlit canopy	19[a]	5	24[a]	4	56[b]	7	54[c]	5	51[c]	3
Non-photosynthetic vegetation	11[a]	3	13[a]	3	4[b]	1	3[bc]	2	2[c]	1
Shade	60[a]	4	56[a]	3	38[b]	5	41[bc]	3	45[d]	4
Exposed soil	10[a]	3	7[a]	2	2[b]	1	2[cd]	1	1.7[d]	1

Note: Different superscript letters represent significant statistical difference among classes using the Tukey test at $p < 0.01$. For example, disturbance and disturbance followed by revegetation showed the same letter (a) meaning that their means are not significantly different using sunlit canopy, whereas ongoing revegetation (b) and revegetation to a stable state (c) showed different letters meaning that there are significant statistical differences among them.

between class means. These statistical results show that sunlit canopy, NPV, shade, and exposed soil fractions are each sensitive to forest disturbance.

Further, to determine canopy cover variability between disturbance classes and assess if a particular stand canopy cover condition will result based on disturbance history, we compared canopy cover estimates between disturbance classes. In this instance, the mean airborne lidar-derived canopy cover showed clear differentiation between disturbance classes (**Figure 8**). The analysis of variance indicated significant differences among the disturbance class canopy cover estimates with $F_{(4245)} = 9.608$, $p < 0.01$. Denser canopy cover was observed in ongoing revegetation and revegetation to stable state classes, whereas canopy cover decreased substantially in disturbance and disturbance followed by revegetation classes (**Figure 8**).

Performance of Landsat spectral indices and SMA endmember fractions for estimating disturbance class canopy structure

Landsat spectral indices (i.e., brightness, greenness, wetness, TCA, TCD, NDVI, and band 5 spectral response data (B5R)) and the SMA endmember fractions (i.e., sunlit canopy, NPV, exposed soil, and shade) were separately
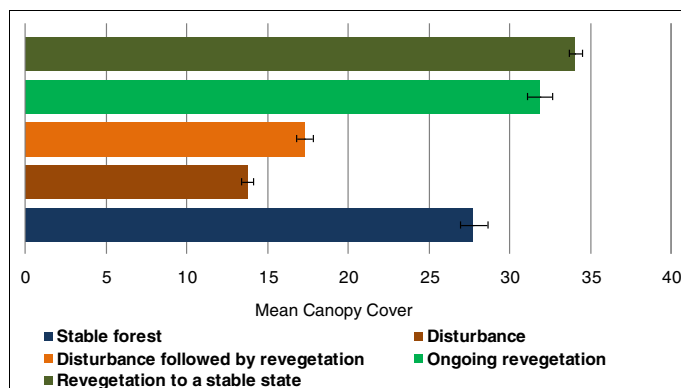

Figure 8. Mean canopy cover summarized in each disturbance class.

modeled to estimate lidar-derived mean canopy cover and height data within each disturbance class using multiple regression. Different errors for estimating lidar-measured canopy cover and height using Landsat spectral characteristics in each forest disturbance class are shown in (**Table 6** and **7**). The canopy cover regression models developed using spectral indices provided better R^2 than those using SMA endmember fractions (**Table 6**). In this study, the best canopy cover estimate of R^2 0.82 and RMSE 0.09 was obtained for the stable forest class using spectral indices. The next best canopy cover estimate of R^2 0.77 and RMSE 0.16 was obtained for the revegetation to a stable state class again using spectral indices. Similarly, independent variables derived from spectral indices resulted a relatively better canopy height estimation than SMA endmembers with the best mean canopy height estimation of R^2 0.67 and RMSE 3.21 obtained for the stable forest class. However, the second best canopy height estimation was obtained using SMA endmembers with R^2 0.60 and RMSE 4.19.

All regression models developed for the stable forest class performed better than those developed for other forest disturbance classes. Overall, improved estimation accuracy was obtained for canopy cover compared with canopy height. In addition, a strong and significant correlation coefficient was obtained for canopy cover ($r = 0.60$), with lower though still significant correlations between lidar-derived canopy height with the Landsat trajectory derived disturbance classes ($r = 0.53$). This suggests a moderately strong relationship between disturbance classes and the predicted variables (canopy cover and height), as expected.

Discussion

Airborne lidar-derived forest canopy structure and time-series of Landsat data were used to relate disturbance class spectral characteristics and terminal canopy structural conditions that characterize forest dynamics in several coastal British Columbia stands. Relatively dense forest stands showed higher Landsat-based TCA values than more open stands or bare soil (see also Gomez et al., 2011; White et al., 2011). Our study has confirmed that, as all Landsat

© 2014 Government of Canada

Table 6. Summary of canopy cover regression models.

Disturbance type	Landsat spectral indices and transformations		SMA endmembers	
	R^2	RMSE	R^2	RMSE
Intact	0.82	0.09	0.71	0.24
Disturbance	0.54	0.36	0.44	0.41
Disturbance followed by revegetation	0.6	0.21	0.49	0.36
Ongoing revegetation	0.74	0.18	0.66	0.31
Revegetation to a stable state	0.77	0.16	0.69	0.31

Table 7. Summary of canopy height regression models.

Disturbance type	Landsat spectral indices and transformations		SMA endmembers	
	R^2	RMSE	R^2	RMSE
Intact	0.67	3.21	0.60	4.19
Disturbance	0.34	1.66	0.27	2.70
Disturbance followed by revegetation	0.42	2.32	0.21	1.54
Ongoing revegetation	0.42	3.25	0.34	2.99
Revegetation to a stable state	0.59	3.59	0.49	2.59

sensors have the requisite bands to generate the greenness and brightness components, TCA is particularly well suited to long-term change detection studies that include MSS data (e.g., Powell et al., 2010).

We used an automated curve-fitting algorithm to detect and label forest disturbance classes using change in Landsat TCA from 1972–2004. The classes included disturbance, disturbance followed by revegetation, ongoing revegetation, and revegetation to a stable state (**Figure 2**). The parameters of the model fully describe the disturbance and recovery dynamics for each pixel, and were used to create a forest disturbance map (**Figure 5**). The implemented validation approach using visual interpretation helped to determine whether the most important parameters (change and no change, disturbance year, and pre-observation disturbance) that are used in the detection of the disturbance classes were accurately identified by the algorithm. All the sampled validation points had relatively high user's and producer's accuracy values. The validation results (**Table 4**) show that the trajectory-based algorithm might miss some minor changes. However, the fact that the majority of the omission errors were attributed to pixels that experienced minor changes after the occurrence of a major change suggests that omission errors for major changes should be low, and therefore biases should be small for those major changes.

The disturbance classes, derived through the trajectory-based disturbance characterization method, can provide a framework for describing the recovery processes of overstory and understory vegetation following stand level disturbance in the study area. The disturbance classes, derived through the trajectory-based disturbance characterization method, can provide a framework for describing the recovery

processes of overstory and understory vegetation following stand level disturbance in the study area. For instance, the disturbance classes can be interpreted in terms of post-disturbance development. In the disturbance and disturbance followed by revegetation classes, stand initiation starts leading to the invasion of new stems on released sites; the ongoing revegetation class, will mostly display vertical stratification and competition among existing and new stems, and understory reinitiation and development of favourable conditions for understory species; the revegetation to stable state class, will mainly include old-growth development and increase in canopy variability and understory development.

The results from the trajectory characterization approach have a variety of potential uses. Because it characterizes disturbance on an annual basis within the available Landsat time series, disturbance events can be more explicitly linked with year-to-year changes for forest management purposes. In addition, by detecting disturbance and recovery stages, the approach provides a better understanding of the evolving landscape for employing various land management techniques. Compared with other currently available disturbance characterization methods the approach used in this study provides easily interpretable parameters. The examination of these parameters and their relationship with forest structure can indicate how disturbance history relates to terminal structure conditions.

However, some concern might arise on the validity of the assumption of this trajectory characterization approach to use an implicit null-hypothesis to identify no-change areas. In addition to the discussed validation results obtained in this study, in response to such concerns previous studies

examined the strength of this assumption by assessing the overall change–no-change agreement between results obtained using this approach and a human interpreter in a mixed forest and they found 90% agreement between the two methods.

In this study SMA was used to extract the spectral characteristics for each disturbance class then the fractions were used to analyse the class separability between the Landsat trajectory derived disturbance classes. First, we compared the endmember abundances among disturbance classes. The fraction images derived from the SMA provided useful information on the disturbance classes spectral characteristics offering a clear distinction between disturbance classes in abundances between sunlit canopy, NPV, shade, and exposed soil. At the scale of disturbance class, the stable and undisturbed forest was characterized by a mixture of sunlit canopy (mean = 51.4%), shade (mean = 44.6%), NPV (mean = 2.3%), and exposed soil (mean = 1.7) (**Figure 7**). The highest green vegetation fraction value was found in the ongoing revegetation class (mean = 56.4%), followed by the revegetation to stable state class (mean = 54.3%). This pattern was interpreted to occur in this area because of the forest gaps caused by disturbance processes. The shade fraction values are typically high across all successional stages. The shade values are a proportional value in the mixture present for each class and can be explained by a number of scenarios, each of which has a spatial and temporal consideration. Following immediately after harvest shade values can be expected to be low. Once succession begins with shrubs and other emergent vegetation, the relationships begin to become more complex. Management activities such as partial harvesting and natural gap development processes will both serve to alter the shade conditions for more mature managed and unmanaged stands. The SMA shows that the sunlit canopy fraction tended to decrease as a function of disturbance recovery (**Figure 7**). Similarly at the lidar scale, this change in sunlit canopy is explained by a decrease in the amount of canopy cover. The mean lidar-derived canopy cover estimates suggest that canopy cover decreased from approximately 34.2% in the ongoing forest regeneration areas to 13.5% in the disturbed areas (**Figure 8**). Although there was a notable decline, canopy cover exhibited little variation between disturbance and disturbance followed by revegetation classes, indicating the slower rate of regeneration within the two classes after disturbance. Similar small amount variations are also shown between the ongoing revegetation and revegetation to stable state classes, signifying the presence of post-disturbance dense canopy cover in these classes. Canopy cover did not reach stable forest equivalence until stands were in the ongoing revegetation and revegetation to stable state classes. The stable forest class shows lower mean canopy cover compared with ongoing revegetation and revegetation to stable state classes, this can be attributed to the more established structure of the stable forest class which

remained intact for the last 40 years or more with the understory areas near gaps having somewhat lower regeneration densities than the ongoing revegetation and revegetation to stable state classes. These disturbed forests tend to have trees closer spaced than intact forests and contain more undergrowth, which might have contributed to the obtained higher mean canopy cover for these two disturbance classes. Overall, denser canopy cover was observed in ongoing revegetation and revegetation to stable state classes, whereas canopy cover decreased substantially in disturbance and disturbance followed by revegetation classes. The analysis of variance conducted in this study indicated significant differences among the disturbance class canopy cover estimates with $F_{(4245)} = 9.608$, $p < 0.01$. Similar to the SMA endmembers, the mean airborne lidar-derived canopy cover showed clear differentiation between the Landsat trajectory derived disturbance classes (**Figure 8**).

Next, to further evaluate if the Landsat trajectory derived disturbance classes could be separated from each other we performed multicomparison of means between the disturbance classes. The result from the pair-wise comparisons of disturbance classes using the Tukey test (**Table 5**) indicates sunlit canopy fraction was not significantly different between stable forest and revegetation to a stable state class. These two classes, however, were significantly different from ongoing revegetation, disturbance followed by revegetation, and disturbance classes. The ongoing revegetation class could also be separated from revegetation to a stable state and stable forest classes with the sunlit canopy fraction. The NPV, shade, and exposed soil fractions showed results similar to the sunlit canopy fraction, except that NPV and shade fractions showed the classes ongoing revegetation and revegetation to stable state were not significantly different from each other. The shade fraction comparisons showed that stable forest class could be separated from revegetation to stable state class. Overall the these statistical results show that sunlit canopy, NPV, shade, and exposed soil fractions are each sensitive to forest disturbance.

In this study, after we used Landsat spectral indices and SMA endmembers to characterize disturbance and to assess the disjunction between the trajectory-based disturbance classes, we found it prudent to evaluate the potential of Landsat spectral indices and SMA fraction images in estimating the terminal canopy structural conditions within each disturbance class and to test their estimation advantage. Both the variables were separately modeled to estimate lidar-derived mean canopy cover and height data in each disturbance class using multiple regression. The results from the regression analysis indicate canopy cover and height regression models developed using spectral indices provided a relatively better estimation than those using SMA endmember fractions (**Tables 6** and **7**). The best canopy cover estimate of R^2 0.82 and RMSE 0.09 was obtained for the stable forest class using spectral indices as independent variables. Compared with the relatively regular structure of

fully grown undisturbed (stable) forests, the other forest disturbance classes typically exhibit complex irregular structure, making it more difficult to accurately estimate their canopy cover and height. As a result, all models developed for the stable forest class, performed better than those developed for other forest disturbance classes. In this study, improved estimation accuracy was obtained for canopy cover compared with canopy height since canopy cover is more closely associated with the two-dimensional satellite data. The best mean canopy height estimation of R^2 0.67 and RMSE 3.21 was obtained for the stable forest class using Landsat spectral indices. Similarly, our results also indicated moderately accurate predictions of lidar-derived canopy height can be obtained using the Landsat-level disturbance class endmember fractions with R^2 0.60 and RMSE 4.19.

The multiple regression analysis indicates accurate predictions of lidar-derived canopy cover can be obtained from the disturbance class Landsat spectral indices and endmember fractions. This indicates an interesting potential for lidar and Landsat integration, with the identification of disturbance classes, to estimate other biophysical properties of disturbed forests. Future work will integrate airborne lidar and Landsat time series data to map forest structure over larger areas and will consider disturbance and recovery trajectories over a broader range of environmental conditions and disturbance types.

Conclusion

In this study, we investigated the use of an automated trajectory-based disturbance characterization method to characterize forest disturbance through the full temporal depth of the Landsat archive. To obtain insights on the linkage between disturbance history and forest structure, we investigated Landsat-derived spectral trajectories as predictive of structural conditions as captured with lidar data. SMA fractions were used to analyse the class separability between the Landsat trajectory derived disturbance classes and the fraction images provided useful information on the disturbance classes spectral characteristics showing clear differentiation in abundances of endmembers between disturbance classes. We also assessed how disturbance history relates to terminal canopy structural conditions by interpreting the relationship between lidar-derived canopy structure and forest disturbance trajectories derived from Landsat time series. Spectral indices and SMA fractions were extracted within Landsat trajectory derived disturbance classes to estimate the terminal canopy structural condition (cover and height) for each disturbance class using multiple regression. This study showed forest structural conditions can be related to a complex suite of stand development trajectories and processes. Our results indicated improved estimates of forest canopy cover and height, particularly for the undisturbed or stable forest stands, can

be obtained using spectral indices. Compared with the relatively regular structure of fully grown undisturbed (stable) forests, the other disturbance classes are found to be more difficult to model due to their complex irregular structure. Based on a comparison with SMA fraction-derived models, the use of spectral indices yielded relatively lower RMSE than SMA fraction-derived models for both canopy cover and height estimates. This study demonstrated the potential of using the 40-year record of Landsat observations to estimate forest canopy cover and height, especially when using pre-stratification of the study area based on disturbance classes.

References

Adams, J.B., Smith, M.O., and Johnson, P.E. 1986. Spectral mixture modeling: A new analysis of rock and soil types at the Viking Lander 1 site. *Journal of Geophysical Research*, Vol. 91, pp. 8098–8112. doi: 10.1029/JB091iB08p08098.

Adams, J.B., Smith, M.O., and Gillespie, A.R. 1993. Imaging spectroscopy: interpretation based on spectral mixture analysis. In *Remote Geochemical Analysis: Elemental and Mineralogical Composition*. ed. V.M. Pieters, and P. Englert. Cambridge University Press, New York. Vol. 7. pp. 145–166.

Adams, J.B., Sabol, D.E., Kapos, V., Almeida, R., Robert, D., Smith, M.O., and Gillespie, A.R. 1995. Classification of multispectral images based on fractions of endmembers: Application to land-cover change in the Brazilian Amazon. *Remote Sensing of Environment*, Vol. 52, pp. 137–154. doi: 10.1016/0034-4257(94)00098-8.

Andersen, H.E., McGaughey, R.J., and Reutebuch, S.E. 2005. Estimating forest canopy fuel parameters using lidar data. *Remote Sensing of Environment*, Vol. 94, pp. 441–449. doi: 10.1016/j.rse.2004.10.013.

Asner, G.P., and Heidebrecht, K.B. 2002. Spectral unmixing of vegetation, soil, and dry carbon cover in arid regions: comparing multispectral and hyperspectral observations. *International Journal of Remote Sensing*, Vol. 23, pp. 3939–3958. doi: 10.1080/01431160110115960.

Canty, M.J., Nielsen, A.A., and Schmidt, M. 2004. Automatic radiometric normalization of multitemporal satellite imagery. *Remote Sensing of Environment*, Vol. 91, pp. 441–451.doi: 10.1016/j.rse.2003.10.024.

Chavez, P. 1996. Image-based atmospheric corrections revisited and improved. *Photogrammetric Engineering and Remote Sensing*, Vol. 62, pp. 1025–1036.

Chen, G., Hay, J.G., Castilla, G., St-Onge, B., and Powers, R. 2010. A multiscale geographic object-based image analysis to estimate lidar measured forest canopy height using Quickbird imagery. *International Journal of Geographical Information Science*, Vol. 25, No. 6, pp. 877–893. doi: 10.1080/13658816.2010.496729.

Chen, G., Hay, G.J., and St-Onge, B. 2012. A GEOBIA framework to estimate forest parameters from lidar transects, Quickbird imagery and machine learning: a case study in Quebec, Canada. *International Journal of Applied Earth Observations and Geoinformation*, Vol. 15, pp. 28–37. doi: 10.1016/j.jag.2011.05.010.

Chen, G., Wulder, M.A., White, J.C., Hilker, T., Coops, N.C. 2012. Lidar calibration and validation for geometric-optical modeling with Landsat imagery. *Remote Sensing of Environment*, Vol. 124, 384–393. doi: 10.1016/j.rse.2012.05.026.

Cohen, W.B., and Goward, S.N. 2004. Landsat's role in ecological applications of remote sensing. *Bioscience*, Vol. 54, pp. 535–545. doi: 10.1641/0006-3568(2004)054[0535:LRIEAO]2.0.CO;2.

Cohen, W.B., Fiorella, M., Gray, J., Helmer, E., and Anderson, K. 1998. An efficient and accurate method for mapping forest clearcuts in the Pacific Northwest using Landsat imagery. *Photogrammetry Engineering and Remote Sensing*, Vol. 64, No. 4, pp. 293–300.

Cohen, W.B., Spies, T.A., Alig, R.A., Oetter, D.R., Maiersperger, T.K., and Fiorella, M. 2002. Characterizing 23 years (1972–95) of stand replacement disturbance in Western Oregon forests with Landsat imagery. *Ecosystems*, Vol. 5, pp. 122–137. doi: 10.1007/s10021-001-0060-X.

Congalton, R. 1991. A review of assessing the accuracy of classifications of remotely sensed data. *Remote Sensing of Environment*, Vol. 37, pp. 35–46. doi: 10.1016/0034-4257(91)90048-B.

Congalton, R.G., and Green, K. 1999. *Assessing the accuracy of remotely sensed data: Principles and practices.* Lewis Publishers, Boca Raton, Fla.

Crist, E.P. 1985. A TM tasseled cap equivalent transformation for reflectance factor data. *Remote Sensing of Environment*, Vol. 17, pp. 301–306. doi: 10.1016/0034-4257(85)90102-6.

Crist, E.P., and Cicone, R.C. 1984. A physically based transformation of Thematic Mapper data—The TM tasseled Cap. *Institute of Electrical and Electronics Engineers Transactions on Geoscience and Remote Sensing*, Vol. 22, No. 23, pp. 256–263.

Dixon, R.K., Brown, S., Houghton, R.A., Solomon, A.M., Trexler, M.C., and Wisniewski, J. 1994. Carbon pools and flux of global forest ecosystems. *Science*, Vol. 263, pp. 185–190. doi: 10.1126/science.263.5144.185.

Dobson, A.P., Bradshaw, A.D., and Baker, A.J.M. 1997. Hopes for the future: restoration ecology and conservation biology. *Science*, Vol. 277, pp. 515–522. doi: 10.1126/science.277.5325.515.

Dolan, K., Masek, J.G., Huang, C., and Sun, G. 2009. Regional forest growth rates combining ICESat GLAS and Landsat data. *Journal of Geophysical Research*, Vol. 114, G00E05.

Donoghue, D.N.M., Watt, P.J., Cox, N.J., and Wilson, J. 2007. Remote sensing of species mixtures in conifer plantations using lidar height and intensity data. *Remote Sensing of Environment*, Vol. 110, pp. 509–522. doi: 10.1016/j.rse.2007.02.032.

Drake, J.B., Knox, R.G., Dubayah, R.O., Clark, D.B., Condit, R., Blair, J.B., and Hofton, M. 2003. Above-ground biomass estimation in closed canopy Neotropical forests using lidar remote sensing: Factors affecting the generality of relationships. *Global Ecology and Biogeography*, Vol. 12, pp. 147–159. doi: 10.1046/j.1466-822X.2003.00010.x.

Duane, M.V., Cohen, W.B., Campbell, J.L., Hudiburg, T., Turner, D.P., and Weyermann, D. 2010. Implications of alternative field-sampling designs on Landsat-based mapping of stand age and carbon stocks in Oregon forests. *Forest Science*. Vol. 56, No. 4, pp. 405–416.

Duncanson, L.I., Niemann, K.O., and Wulder, M.A. 2010. Estimating forest canopy height and terrain relief from GLAS waveform metrics. *Remote Sensing of Environment*, Vol. 114, pp. 138–154. doi: 10.1016/j.rse.2009.08.018.

Elmore, A.J., Mustard, J.F., Manning, S.J., and Lobell, D.B. 2000. Quantifying vegetation change in semiarid environments: precision and accuracy of spectral mixture analysis and the normalised difference vegetation index. *Remote Sensing of Environment*, Vol. 73, pp. 87–102. doi: 10.1016/S0034-4257(00)00100-0.

Falkowski, M.J., Evans, J.S., Martinuzzi, S., Gessler, P.E., and Hudak, A.T. 2009. Characterizing forest succession with lidar data: An evaluation for the Inland Northwest, USA. *Remote Sensing of Environment*, Vol. 113, pp. 946–956. doi: 10.1016/j.rse.2009.01.003.

Gao, F., Masek, J.G., and Wolfe, R.E. 2009. Automated registration and orthorectification package for Landsat and Landsat-like data processing. *Journal of Applied Remote Sensing*, Vol. 3, p. 33515. doi: 10.1117/1.3290811.

Garcia-Haro, F.J., Gilabert, M.A., and Melia, J. 1999. Extraction of endmembers from spectral mixtures. *Remote Sensing of Environment*, Vol. 68, pp. 237–253. doi: 10.1016/S0034-4257(98)00115-1.

Goetz, S.J., Baccini, A., Laporte, N.T., Johns, T., Walker, W., and Kellndorfer, J. 2009. Mapping and monitoring carbon stocks with satellite observations: A comparison of methods. *Carbon Balance and Management*, Vol. 4, p. 2. doi: 10.1186/1750-0680-4-2.

Gillanders, S.N., Coops, N.C., Wulder, M.A., Gergel, S.E., and Nelson, T. 2008. Multitemporal remote sensing of landscape dynamics and pattern change: Describing natural and anthropogenic trends. *Progress in Physical Geography*, Vol. 35, No. 5, pp. 502–528.

Gomez, C., White, J.C., Wulder M.A. 2011. Characterizing the state and processes of change in a dynamic forest environment using hierarchical spatio-temporal segmentation. *Remote Sensing of Environment*, Vol. 115, pp. 1665–1679. doi: 10.1016/j.rse.2011.02.025.

Goodale, C.L., Apps, M.J., Birdsey, R.A., Field, C.B., Heath, L.S., and Houghton, R.A. 2002. Forest carbon sinks in the Northern Hemisphere. *Ecological Applications*, Vol. 21, pp. 891–899. doi: 10.1890/1051-0761(2002)012[0891:FCSITN]2.0.CO;2.

Goodwin, N., Coops, N.C., and Stone, C. 2005. Assessing plantation canopy condition from airborne imagery using spectral mixture analysis and fractional abundances. *International Journal of Applied Earth Observation and Geoinformation*, Vol. 7, pp. 11–28. doi: 10.1016/j.jag.2004.10.003.

Hall, F.G., Bergen, K., Blair, J.B., Dubayah, R., Houghton, R., Hurtt, G. 2011. Characterizing 3D vegetation structure from space: Mission requirements. *Remote Sensing of Environment*, Vol. 115, pp. 2753–2775. doi: 10.1016/j.rse.2011.01.024.

Hansen, M.J., Franklin, S.E., Woudsma, C.G., and Peterson, M. 2001. Caribou habitat mapping and fragmentation analysis using Landsat MSS, TM, and GIS data in the North Columbia Mountains, British Columbia, Canada. *Remote Sensing of Environment*, Vol. 77, pp. 50–65. doi: 10.1016/S0034-4257(01)00193-6.

Healey, S.P., Cohen, W.B., Zhiqiang, Y., and Krankina, O. 2005. Comparison of Tasseled Cap-based Landsat data structures for forest disturbance detection. *Remote Sensing of Environment*, Vol. 97, No. 3, pp. 301–310. doi: 10.1016/j.rse.2005.05.009.

Healey, S.P., Yang, Z., Cohen, W.B., and Pierce, D.J. 2006. Application of two regression based methods to estimate the effects of partial harvest

on forest structure using Landsat data. *Remote Sensing of Environment*, Vol. 101, pp. 115–126. doi: 10.1016/j.rse.2005.12.006.

Helmer, E.H., Ruzycki, T.S., Wunderle Jr., J.M., Vogesser, S., Ruefenacht, B., Kwit, C., Brandeis, T.J., and Ewert, D.N. 2010 Mapping tropical dry forest height, foliage height profiles and disturbance type and age with a time series of cloud-cleared Landsat and ALI image mosaics to characterize avian habitat. *Remote Sensing of Environment*, Vol. 114, pp. 2457–2473. doi: 10.1016/j.rse.2010.05.021.

Hilker, T., Wulder, M.A., and Coops, N.C. 2008. Update of forest inventory data with lidar and high spatial resolution satellite imagery. *Canadian Journal of Remote Sensing*, Vol. 34, pp. 5–12. doi: 10.5589/m08-004.

Huang, C., Goward, S.N., Schleeweis, K., Thomas, N., Masek, J.G., and Zhu, Z. 2009. Dynamics of national forests assessed using the Landsat record: Case studies in eastern United States. *Remote Sensing of Environment*, Vol. 113, pp. 1430–1442. doi: 10.1016/j.rse.2008.06.016.

Huang, C., Wylie, B., Yang, L., Homer, C., and Zylstra, G. 2002. Derivation of a Tasselled Cap Transformation based on Landsat 7 at-satellite reflectance. *International Journal of Remote Sensing*, Vol. 23, No. 8, pp. 1741–1748. doi: 10.1080/01431160110106113.

Hudak, A.T., Lefsky, M.A., Cohen, W.B., and Berterreche, M. 2002. Integration of lidar and Landsat ETM + data for estimating and mapping forest canopy height. *Remote Sensing of Environment*, Vol. 82, pp. 397–416. doi: 10.1016/S0034-4257(02)00056-1.

Hutchinson, M.F. 1989. A new procedure for gridding elevation and stream line data with automatic removal of spuriouspits. *Journal of Hydrology*, Vol. 106, pp. 3–4. doi: 10.1016/0022-1694(89)90073-5.

Hyde, P., Dubayah, R., Peterson, B., Blair, J.B., Hofton, M., Hunsaker, C., Knox, R., and Walker, W. 2005. Mapping forest structure for wildlife habitat analysis using waveform lidar: validation of montane ecosystems. *Remote Sensing of Environment*, Vol. 96, pp. 427–437. doi: 10.1016/j.rse.2005.03.005.

Jin, S., and Sader, S.A. 2005. Comparison of time series Tasseled Cap wetness and the normalized difference moisture index in detecting forest disturbances. *Remote Sensing of Environment*, Vol. 94, pp. 364–372. doi: 10.1016/j.rse.2004.10.012.

Kennedy, R.E., Cohen, W.B., and Schroeder, T.A. 2007. Trajectory-based change detection for automated characterization of forest disturbance dynamics. *Remote Sensing of Environment*, Vol. 110, No. 3, pp. 370–386. doi: 10.1016/j.rse.2007.03.010.

Lal, R. 1997. Deforestation effects on soil degradation and rehabilitation in western Nigeria. *Land Degradation and Development*, Vol. 8, No. 2, pp. 95–126.

Li, A., Huang, C., Sun, G., Shi, A., Toney, C., Zhu, Z., Rollins, M.G., Goward, S.N., and Masek, J.G. 2011. Modeling the height of young forests regenerating from recent disturbances in Mississippi using Landsat and ICESat data, *Remote Sensing of Environment*, Vol. 115, pp. 1837–1849.

Lobell, D.B., Asner, G.P., Law, B.E., and Treuhaft, R.N. 2002. View angle effects on canopy reflectance and spectral mixture analysis of coniferous forests using AVIRIS. *International Journal of Remote Sensing*, Vol. 23, No. 11. pp. 2247–2262. doi: 10.1080/01431160110075613.

Lu, D., Batistellas, M., Moran, E., and Mausel, P., 2004. Application of spectral mixture analysis to Amazonian land-use and land-cover classification. *International Journal of Remote Sensing*, Vol. 25, No. 23, pp. 5345–5358. doi: 10.1080/01431160412331269733.

Lu, D., Mausel, P., Brondizio, E., and Moran, E. 2004. Change detection techniques. *International Journal of Remote Sensing*, Vol. 25, No. 12, pp. 2365–2407. doi: 10.1080/0143116031000139863.

Lunetta, R., Johnson, D.M., Lyon, J., and Crotwell, J. 2004. Impacts of imagery temporal frequency on land-cover change detection monitoring. *Remote Sensing of Environment*, Vol. 89, pp. 444–454. doi: 10.1016/j.rse.2003.10.022.

Markwardt, C.B. 2008. Non-Linear Least Squares Fitting in IDL with MPFIT. In *Astronomical Data Analysis Software and Systems Conference Series XVIII*. November 2–5, Quebec City, Canada. ed. D. Bohlender, P. Dowler, and D. Durand. Vol. 411, p. 251.

Masek, J.G., Huang, C.H., Wolfe, R., Cohen, W., Hall, F., and Kutler, J. 2008. North American forest disturbance mapped from a decadal Landsat record. *Remote Sensing of Environment*, Vol. 112, pp. 2914–2926. doi: 10.1016/j.rse.2008.02.010.

McRoberts, R.E., Stahl, G., Vidal, C., Lawrence, M., Tomppo, E.O., Schadauer, K., Chirici, G., and Bastrup-Birk, A. 2010. National forest inventories: prospects for harmonised international reporting. In *National Forest Inventories. Pathways for Common Reporting*. ed. E. Tomppo, T. Gschwantner, M. Lawrence, and R.E. McRoberts. Springer, Heidelberg, pp. 33–44.

Morgenstern, K., Black, A., Humphreys, E.R., Griffis, T.J., Gordon, B.Drewitt, J.B., Cai, T., Nesic, Z., Spittlehouse, D.L., and Livingston, N.J. 2004. Sensitivity and uncertainty of the carbon balance of a Pacific Northwest Douglas-fir forest during an El Nino/La Nina cycle. *Agricultural and Forest Meteorology*, Vol. 123, pp. 201–219. doi: 10.1016/j.agrformet.2003.12.003.

Morsdorf, F., Kotz, B., Meier, E., Itten, K.I., and Allgower, B. 2006. Estimation of LAI and fractional cover from small footprint airborne laser scanning data based on gap fraction. *Remote Sensing of Environment*, Vol. 104, No. 1, pp. 50–61. doi: 10.1016/j.rse.2006.04.019.

Morsdorf, F., Marell, A., Koetz, B., Cassagne, N., Pimont, F., and Rigolot, E. 2010. Discrimination of vegetation strata in a multi-layered Mediterranean forest ecosystem using height and intensity information derived from airborne laser scanning. *Remote Sensing of Environment*, Vol. 114, pp. 1403–1415. doi: 10.1016/j.rse.2010.01.023.

Ott, L. 1992. *An introduction to statistical methods and data analysis (4th edition)*. Duxbury Press, Belmont, California.

Pascual, C., Garcia, A., Cohen, W.B., and Martin, S. 2010. Relationship between lidar-derived forest canopy height and Landsat images. *International Journal of Remote Sensing*, Vol. 31, pp. 1261–1280. doi: 10.1080/01431160903380656.

Peddle, D.R., Hall, F.G., and LeDrew, E.F. 1999. Spectral mixture analysis and geometric-optical reflectance modelling of boreal forest biophysical structure. *Remote Sens. Environ*, Vol. 67, pp. 288–297.

Pflugmacher, D., Cohen, W.B., Kennedy, R.E. 2012. Using Landsat-derived disturbance history (1972–2010) to predict current forest structure. *Remote Sensing of Environment*, Vol. 122, pp. 146–165. doi: 10.1016/j.rse.2011.09.025.

Powell, S.L., Cohen, W.B., Yang, Z., Pierce, J.D., and Alberti, M. 2008. Quantification of impervious surface in the Snohomish Water Resources Inventory Area of Western Washington from 1972–2006. *Remote Sensing of Environment*, Vol. 112, pp. 1895–1908.

Powell, S.L., Cohen, W.B., Healey, S.P., Kennedy, R.E., Moisen, G.G., Pierce, K.B., and Ohmann, J.L. 2010. Quantification of live aboveground forest biomass dynamics with Landsat time-series and field inventory data: A comparison of empirical modeling approaches. *Remote Sensing*

of Environment, Vol. 114, No. 5, pp. 1053–1068. doi: 10.1016/j.rse.2009.12.018.

Pregitzer, K.S., and Euskirchen, E.S. 2004. Carbon cycling and storage in world forests: biome patterns related to forest age. *Global Change Biology*, Vol. 10, No. 12, pp. 2052–2077. doi: 10.1111/j.1365-2486.2004.00866.x.

Price, K.P., and Jakubauskas, M.E. 1998. Spectral retrogression and insect damage in lodgepole pine successional forests. *International Journal Remote Sensing*, Vol. 19, pp. 1627–1632. doi: 10.1080/014311698215405.

Schroeder, T.A., Cohen, W.B., Song, C., Canty, M.J., and Yang, Z. 2006. Radiometric correction of multi-temporal Landsat data for characterization of early successional forest patterns in western Oregon. *Remote Sensing of Environment*, Vol. 103, pp. 16–26. doi: 10.1016/j.rse.2006.03.008.

Schroeder, T.A., Cohen, W.B., and Zhiqiang, Y. 2007. Patterns of Forest regrowth following clearcutting in Western Oregon as determined from Landsat time-series. *Forest Ecology and Management*, Vol. 243, pp. 259–273. doi: 10.1016/j.foreco.2007.03.019.

Smith, A.M.S., Falkowski, M.J., Hudak, A.T., Evans, J.S., Robinson, A.P., and Steele, C.M. 2009. A cross-comparison of field, spectral, and lidar estimates of forest canopy cover. *Canadian Journal of Remote Sensing*, Vol. 35, No. 5, pp. 447–459. doi: 10.5589/m09-038.

Smith, M.O., Ustin, S.L., Adams, I.B., and Gillespie, A.R. 1990. Vegetation in deserts: I. A regional measure of abundance from multispectral images. *Remote Sensing of Environment*, Vol. 31, pp. 1–26. doi: 10.1016/0034-4257(90)90074-V.

Smith, M.O., Adams, I.B., and Sabol, D.E. 1994. Spectral mixture analysis-new strategies for the analysis of multi spectral data. In *Imaging Spectrometry-A Tool for Environment Observations*. ed. I. Hill, and I. Megier. Kluwer Academic Publishers, Massachusetts, pp. 125–144.

Solberg, S., Næsset, E., Hanssen, K.H., and Christiansen, E. 2006. Mapping defoliation during a severe insect attack on Scots pine using airborne laser scanning. *Remote Sensing of Environment*, Vol. 102, pp. 364–376. doi: 10.1016/j.rse.2006.03.001.

Somers, B., Asner, G.P., Tits, L., and Coppin, P. 2011. Endmember variability in Spectral Mixture Analysis: A review. *Remote Sensing of Environment*, Vol. 115, pp. 1603–1616. doi: 10.1016/j.rse.2011.03.003.

Song, C., Woodcock, C.E., Seto, K.C., Lenney, M.P., and Macomber, S.A. 2001. Classification and change detection using Landsat data: when and how to correct atmospheric effects? *Remote Sensing of Environment*, Vol. 75, pp. 230–244. doi: 10.1016/S0034-4257(00)00169-3.

Song, C., Schroeder, T.A., Cohen, W.B. 2007. Predicting temperate conifer forest successional stage distributions with multitemporal Landsat Thematic Mapper imagery. *Remote Sensing of Environment*, Vol. 106, pp. 228–237. doi: 10.1016/j.rse.2006.08.008.

Souza, C., Firestone, L., Silva, L.M., Roberts, D. 2003. Mapping forest degradation in the Eastern Amazon from SPOT 4 through spectral mixture models. *Remote Sensing of Environment*, Vol. 87, pp. 494–506. doi: 10.1016/j.rse.2002.08.002.

Stehman, S.V., and Czaplewski, R.L. 1998. Design and analysis for thematic map accuracy assessment: Fundamental principles. *Remote Sensing of Environment*, Vol. 64, pp. 331–344. doi: 10.1016/S0034-4257(98)00010-8.

Strahler, A.H., Woodcock, C.E., and Smith, J.A. 1986. On the nature of models in remote sensing. *Remote Sensing of Environment*, Vol. 20, pp. 121–139. doi: 10.1016/0034-4257(86)90018-0.

Tompkins, S., Mustard, J.F., Pieters, C.M., and Forsyth, D.W. 1997. Optimization of 705 endmembers for spectral mixture analysis. *Remote Sensing of Environment*, Vol. 59, pp. 472–489. doi: 10.1016/S0034-4257(96)00122-8.

White, J.C., Wulder, M.A., Gomez, C., and Stenhouse, G. 2011. A history of habitat dynamics: Characterizing 35 years of stand replacing disturbance. *Canadian Journal of Remote Sensing*, Vol. 37, No. 2, pp. 234–251. doi: 10.5589/m11-034.

Wulder, M.A., and Franklin, S.E. 2007. *Understanding Forest Disturbance and Spatial Pattern: Remote Sensing and GIS Approaches*. Taylor and Francis, Boca Raton, Florida.

Wulder, M.A., and Seemann, D. 2003. Forest inventory height update through the integration of lidar data with segmented Landsat imagery. *Canadian Journal of Remote Sensing*, Vol. 29, pp. 536–543. doi: 10.5589/m03-032.

Wulder, M.A., Franklin, S.E., and White, J.C. 2004. Sensitivity of hyper clustering and labelling land cover classes to Landsat image acquisition date. *International Journal of Remote Sensing*, Vol. 10, pp. 5337–5344. doi: 10.1080/0143116042000192385.

Wulder, M.A., White, J.C., Bentz, C., Alvarez, M.F., and Coops, N. 2006. Estimating the probability of mountain pine beetle red attack damage. *Remote Sensing of Environment*, Vol. 101, No. 2, pp. 150–166. doi: 10.1016/j.rse.2005.12.010.

Zeng, Y., Schaepman, M.E., Wu, B., Clevers, J., and Bregt, A. 2007. Quantitative forest canopy structure assessment using an inverted geometric-optical model and up-scaling. *International Journal of Remote Sensing*, Vol. 30, pp. 1385–1406. doi: 10.1080/01431160802395276.

Zhao, K.G., and Popescu, S. 2009. Lidar-based mapping of leaf area index and its use for validating GLOBCARBON satellite LAI product in a temperate forest of the southern USA. *Remote Sensing of Environment*, Vol. 113, pp. 1628–1645. doi: 10.1016/j.rse.2009.03.006.

Zhu, Z., Woodcock, C.E. 2011. Object-based cloud and cloud shadow detection in Landsat imagery. *Remote Sensing of Environment*, Vol. 118, pp. 83–94. doi: 10.1016/j.rse.2011.10.028.